JGR Oceans

RESEARCH ARTICLE
10.1029/2021JC018066

The Role of Summer Snowstorms on Seasonal Arctic Sea Ice Loss

Won-Il Lim[1], Hyo-Seok Park[2], Alek A. Petty[3], and Kyong-Hwan Seo[1]

[1]Department of Atmospheric Sciences, Pusan National University, Busan, South Korea, [2]Department of Ocean Science and Technology, Hanyang University, Ansan, South Korea, [3]Cryospheric Sciences Laboratory, NASA Goddard Space Flight Center, Greenbelt, MD, USA

Key Points:

- Summer Arctic snowstorms result in positive sea ice extent and albedo anomalies due to associated changes in ice drift and air cooling
- Sea ice-ocean model experiments suggest that snowstorm–induced surface air cooling is the dominant driver of reduced seasonal sea ice loss
- Reductions in the prevalence and severity of summer Arctic snowstorms could accelerate future Arctic sea ice loss

Supporting Information:

Supporting Information may be found in the online version of this article.

Correspondence to:

H.-S. Park and K.-H. Seo,
hspark1@gmail.com;
khseo@pusan.ac.kr

Citation:

Lim, W.-I., Park, H.-S., Petty, A. A., & Seo, K.-H. (2022). The role of summer snowstorms on seasonal Arctic sea ice loss. *Journal of Geophysical Research: Oceans*, *127*, e2021JC018066. https://doi.org/10.1029/2021JC018066

Received 29 SEP 2021
Accepted 21 NOV 2022

Author Contributions:

Conceptualization: Hyo-Seok Park, Alek A. Petty, Kyong-Hwan Seo
Formal analysis: Won-Il Lim
Funding acquisition: Hyo-Seok Park
Investigation: Won-Il Lim, Hyo-Seok Park, Alek A. Petty
Methodology: Won-Il Lim, Hyo-Seok Park, Alek A. Petty
Resources: Hyo-Seok Park, Kyong-Hwan Seo
Supervision: Hyo-Seok Park, Kyong-Hwan Seo
Validation: Won-Il Lim, Alek A. Petty
Visualization: Won-Il Lim

Abstract In the Arctic, short-lived summer snowstorms can provide snow cover that can increase surface reflectivity and heat capacity. Despite their potential importance, little research has been done to understand the impact of summer snowstorms on basin-scale Arctic sea ice cover. Our observational analysis shows that a summer snowstorm event is accompanied by cyclonic ice drift, increases in surface albedo and surface air cooling that can persist for up to ~2 weeks, dampening sea ice loss. Specifically, multiple snowstorm events in a summer, on average, results in net increase in sea ice extent of $\sim 0.2 \times 10^6$ km^2 by early September. Experiments with a sophisticated ice-ocean model framework indicate that the initial expansion of sea ice extent is driven by cyclonic wind-driven ice drifts driving sea ice southwards and increasing albedo around the summer ice edge, however the thermal effects from the associated snowfall and atmospheric conditions result in a stronger overall impact on basin-averaged sea ice extent at seasonal scales. Additional model experiments were carried out to isolate the physical processes contributing to the thermal response of Arctic sea ice to summer snowstorms. Our results show the impact of surface air cooling on sea ice extent is about 3.5 times larger than the snowfall/albedo response. However, our simulated albedo response is weaker than the observed response, likely due to the negligible difference in surface albedo between old snow and freshly fallen snow—a limiting factor in our analysis and a topic worthy of future focus.

Plain Language Summary In this study we seek to better understand the impact on summer Arctic sea ice cover from short-lived summer snowstorms. We use satellite-derived observational data to show that summer snowstorms in the Arctic are accompanied by surface air cooling, increases in sea ice cover, and increases in averaged Arctic Ocean surface reflectivity (sea ice is more reflective than the ocean). Using a sophisticated sea ice-ocean model and targeted sensitivity studies, we quantify the impact of summer Arctic snowstorms on sea ice, showing that multiple summer snowstorms can substantially increase the end of summer Arctic sea ice extent. Additional model experiments suggest that surface air cooling associated with a given summer snowstorm plays a bigger role in reducing sea ice loss compared to the direct impact of snowfall and increases in reflectance. Snowstorms are also associated with anti-clockwise winds and ice drifts that push Arctic sea ice southwards, increasing sea ice cover and surface reflectance around the ice edge but decreasing sea ice cover and reflectance within the Central Arctic. Our findings suggest that the continued warming of the Arctic and decreases in summer snowfall could play an important role in accelerating Arctic sea ice decline in future decades.

1. Introduction

The Arctic near-surface atmosphere has warmed at more than twice the rate of the global average over recent decades, while summer sea ice coverage has reduced by around 50% (Walsh, 2014). The positive ice-albedo feedback along with several other feedback mechanisms have contributed to these rapid changes (Goosse et al., 2018; Serreze & Barry, 2014). Because the Arctic climate is generally dry, where column-integrated water vapor on seasonal time scales is less than ~20 mm even in the wettest summer (Rinke et al., 2019; Serreze & Barry, 2014; Serreze et al., 1995), winter snow accumulation is generally limited to ~20–30 cm in the Eurasian and the Pacific Seas (Petty et al., 2018; Shalina & Sandven, 2018; Webster et al., 2019). As sunlight returns to the Arctic Ocean in spring, dry snow turns to wet snow/ponded ice and bare ice is exposed when the snow completely melts and drains (Ehn et al., 2006; Grenfell & Maykut, 1977; Perovich et al., 2002).

Writing – original draft: Won-Il Lim, Hyo-Seok Park, Alek A. Petty
Writing – review & editing: Won-Il Lim, Hyo-Seok Park, Alek A. Petty, Kyong-Hwan Seo

Snow over sea ice is an excellent thermal insulator that prevents ice melting from sunlight until snow is melted away. Moreover, because the albedo of melting snow (0.8–0.5) and ponded ice (0.1–0.6) is much lower than that of cold, snow covered sea ice (>0.8) (Grenfell & Maykut, 1977; Perovich & Polashenski, 2012; Perovich et al., 2002), snow can substantially reduce the absorption of sunlight by sea ice until late spring and early summer. The timing of spring snow melt and/or the coverage of melt ponds over sea ice is thus thought to be a contributing factor to seasonal Arctic sea ice loss (Petty et al., 2017; Schröder et al., 2014; Webster et al., 2018).

While the seasonal snow cover is expected to largely melt out each year (Hezel et al., 2012; Warren et al., 1999), leaving behind either melt ponds or bare ice, summer snowstorms can provide ephemeral snow cover which can delay melt onset. In the Arctic, storms are most prevalent in summer (Screen et al., 2011; Serreze & Barrett, 2008; Simmonds et al., 2008) and multiple reanalysis data consistently indicate that there are more snowfall than rainfall over the central Arctic Ocean in summer (Figure S1 in Supporting Information S1). A recent case study found that a summer Arctic snowstorm event in early June in the Chukchi Sea delayed melt onset by ∼11 days (Perovich et al., 2017). The results of Perovich et al. (2017) showed that a single summer snowstorm can provide a strong influence on large-scale surface albedo, surface turbulent heat flux and sea ice conditions, but research into these effects is still lacking.

Using atmospheric and sea ice data from observations and reanalyzes, we show that summer snowstorm events are accompanied by increasing sea ice albedo, persistent surface air cooling, increased surface turbulent heat fluxes and positive sea ice extent anomalies. Using an ocean-sea ice model, we aim to disentangle the dynamics and thermodynamic effects on sea ice during the summer snowstorms.

2. Materials and Methods

2.1. Observations and Reanalysis Data

2.1.1. Observations

All the observation and reanalysis data used in this study are summarized in Table 1. To identify the response of Arctic sea ice cover, we use satellite-observed daily sea ice concentration (SIC) data at a nominal 25 by 25 km polar stereographic grid resolution (Meier et al., 2017) and a daily aggregated Arctic sea ice extent index (Fetterer et al., 2017) provided by the National Snow and Ice Data Center (NSIDC). NSIDC provides SIC using data collected through Scanning Multichannel Microwave Radiometer, the Special Sensor Microwave Imager, and Special Sensor Microwave Imager/Sounder. SIC data are produced by the Climate Data Recording algorithm, a combination of two algorithms that characterize the spectral behavior of ice or open water NASA Team (Cavalieri et al., 1984) and Bootstrap (Comiso, 1986).

To assess surface air temperature (Tsfc) over Arctic sea ice, we use data obtained from the Atmospheric Infrared Sounder on NASA's Aqua satellite (AIRS; Aumann et al., 2003) spanning 2003–2019. AIRS is a 2,378 spectral channel infrared spectrometer/radiometer measuring a 3.7–15.4 μm spectral range and has a ∼13.5 km horizontal resolution at nadir.

To identify the observed response of downward radiations and albedo accompanying snowstorms, we use the Clouds and the Earth's Radiant Energy System (CERES) Synoptic 1° × 1° (SYN1deg) product (Doelling et al., 2013) from 2000 to 2019. The surface fluxes in SYN1deg are computed from geostationary satellite (GEO) retrievals (e.g., cloud optical depth and height) of the Goddard Earth Observing System Data Assimilation System (GEOS) version 5.4.1 (Suarez et al., 2008). Cloud and aerosol properties are derived from Moderate Resolution Imaging Spectroradiometer and geostationary satellites. The cloud liquid water of SYN1deg has been extensively verified through satellite data such as the Advanced Microwave Scanning Radiometer-Earth Observing System sensor on NASA's Aqua satellite (Minnis et al., 2011) and ground-based measurements such as Atmospheric Radiation Measurement (Dong et al., 2008). The Arctic summer surface radiative flux biases of CERES are generally within ∼15 W m^{-2} (Huang et al., 2022). The albedo of CERES SYN1deg over sea ice tends to be slightly underestimated. Comparisons with in situ observations from the Tara drifting (Riihelä et al., 2017) and the Multidisciplinary drifting Observatory for the Study of Arctic Climate (Huang et al., 2022) indicate that CERES SYN1deg underestimates summer upwelling shortwave radiation over sea ice by around 5%. However, the temporal variability of CERES albedo matches well with in situ observations (Riihelä et al., 2017).

Table 1
Time Periods and Variables of Each Observation and Reanalysis Data

Product	Time span	Variables	Product type
CERES	2000–2019	$SW^{\downarrow}$, $SW^{\uparrow}$, $LW^{\downarrow}$	Observation
AIRS	2003–2019	T2m	Observation
NSIDC	1980–2019	SIC, sea ice drift	Observation
JRA55	1980–2019	Snowfall, rainfall, T2m, $SW^{\downarrow}$, $SW^{\uparrow}$, SHF, LHF, SLP, 10 m-winds	Reanalysis
MERRA2	1980–2019	Snowfall, rainfall, T2m, $SW^{\downarrow}$, $SW^{\uparrow}$, SHF, LHF	Reanalysis
ERA5	1980–2019	Snowfall, rainfall, T2m, $SW^{\downarrow}$, $SW^{\uparrow}$, SHF, LHF	Reanalysis
CICE5 (model simulation results)	1980–2019	SIC, sea ice drift, snow depth, ice thickness, Tsfc, $SW^{\downarrow}$, $SW^{\uparrow}$	Model

To identify sea ice drift anomalies, we use satellite-observed sea ice motion data from the Polar Pathfinder Version 4 Daily Sea Ice Motion Vectors product (M. A. Tschudi et al., 2019), which provides daily data spanning October 1978 to December 2020. Satellite-derived sea ice drift data can include significant uncertainties at synoptic time-scales, especially in the summer when surface melt affects the passive microwave identification of ice parcels (Sumata et al., 2014; M. Tschudi et al., 2020). The uncertainty range of the satellite-observed sea ice drift speed is 1.0–1.8 cm s^{-1} in Arctic summer (Sumata et al., 2015).

2.1.2. Reanalysis Data

Because there is no observed snowfall data that can cover the basin-scale Arctic Ocean in summer, we instead assess snowfall estimates from multiple reanalyzes. To identify atmospheric circulations during snowstorm events, we also investigate sea level pressure (SLP) and 10 m winds from the reanalyzes. To identify the thermal effects during snowstorm events, we examine 2 m air temperature (T2m), downward shortwave and longwave radiations, upward shortwave radiation, surface latent heat flux (LHF), and surface sensible heat flux (SHF). Among these variables, T2m, downward shortwave and longwave radiations are also used to force our sea ice-ocean model. In this study, we use three reanalysis products: the Japanese 55-year Reanalysis (JRA55; Kobayashi et al., 2015), the European Center for Medium-Range Weather Forecasts version 5 (ERA5; Hersbach et al., 2020), and the modern-era retrospective analysis for research and applications version 2 (MERRA2; Gelaro et al., 2017).

2.2. Methods

2.2.1. Definition of Snowstorms

In this study, we define a *snowstorm event* when the daily snowfall averaged over the Eurasian-Pacific sector of the Arctic (80–240°E; 69–90°N) exceeds 0.75 standard deviations for 3 or more consecutive days. Here, "standard deviation" is the daily standard deviation calculated from 40 summers (June-July-August), which is a total of 3,680 days from 1980 to 2019. We focus on snowstorms over the Eurasian-Pacific sector of the Arctic that can have a strong influence on the basin-scale summer Arctic sea ice cover compared to North Atlantic storm activity (Serreze & Barrett, 2008; Simmonds et al., 2008). Our snowstorm definition was guided by the study of Perovich et al. (2017) that assessed the impact of a relatively heavy snowstorm with observed snowfall of around ~5 cm day^{-1} for 4 consecutive days in early June 2014. The climatological mean lifetimes of summer Arctic storms are about 3–7 days (Sepp & Jaagus, 2010; X. Zhang et al., 2004).

The number of summer snowstorm events detected from 1980 to 2019 from JRA55, ERA5, and MERRA2 are 95, 96, and 96, respectively. Lag day 0 is defined as the peak snowfall day averaged over the Eurasian-Pacific sector. The lagged composites of the areal-averaged snowfall show that snowfall sharply increases from lag day −2 and sharply decreases after peaking at lag day 0 (Figure S2 in Supporting Information S1). While the majority of our snowstorms are relatively short in duration, generally less than 5 days, several snowstorms show significantly longer durations. Summer snowstorms persisting for 5 days or more make up ~36% and ~30% of the total number of summer snowstorm events in JRA55 and MERRA2, respectively. The composite maps of accumulated snowfall during the snowstorm events show that the snowfall accumulates over wide areas of the Arctic, more than 5 mm day^{-1} in snow water equivalent (*s.w.e.*) over the Central Arctic Ocean (Figure S2 in Supporting Information S1). Here, the accumulated snowfall implies the integration of daily snowfall from lag day −7 to day +7.

2.2.2. Composite Analysis

While the majority of satellite observations and reanalysis products start from year 1979/1980, several satellite observations are available only after 2000. Daily surface radiation data from CERES are available since 2000, whereas surface air temperature data of AIRS are available since 2003. For surface radiations and albedo, the analysis period is from 2000 to 2019 both for CERES and reanalysis data. In this time period, we detect 47 snowstorm events in JRA55. Likewise, the analysis period for surface air temperature is from 2003 to 2019, which includes 36 snowstorm events. In this study, we removed the long-term trends of all the variables prior to generating our spatial composites. We tested statistical significance using Student's two-tailed *t* test at the 95% significance level.

2.3. Idealized Ice-Ocean Model Experiment

We utilized an ice-ocean coupled model within the Community Earth System Model version 2 framework (Danabasoglu et al., 2020) to quantify the effects of surface wind and snowfall anomalies on sea ice cover during snowstorm events. The ocean and sea-ice components are the second version of the second version of the Parallel Ocean Program (POP; Smith et al., 2010) and the Community Ice Code version 5 (CICE5) sea ice model version 5.1.2 (Hunke et al., 2015). POP2 has a dipolar displaced pole grid centered at Greenland with 1° nominal resolution (gx1v7) and monotonically increasing 60 vertical levels from 10 to 250 m. CICE5.1.2 use a mushy-layer thermodynamics (Feltham et al., 2006; Turner & Hunke, 2015), which reflect a prognostic vertical salinity profile within the ice, and improved melt pond parametrization (Hunke et al., 2013). The CICE5.1.2 has the same resolution as POP2.

The ocean-ice coupled model simulation is forced using JRA55-do atmospheric data (Tsujino et al., 2018), which is based on JRA55. The JRA55-do is improved over the Coordinated Ocean-ice Reference Experiment-interannual forcing (Griffies et al., 2009) with spatial and temporal resolution and greater self-consistency between forced fields. JRA55-do has been proposed as the new standard global ocean-ice model forcing for hindcast simulations including the Ocean Model Intercomparison Project (Griffies et al., 2016). JRA55-do includes 3-hourly atmospheric variables (surface temperature, humidity, winds, and SLP), radiative fluxes (downward longwave and shortwave), precipitation and daily run off variables from 1958 to the present. CICE5 calculates snowfall and rainfall rates explicitly based on total precipitation and surface air temperature forcings. CICE5–simulated snowfall using the JRA55-do forcing is ∼35% lower than that of JRA55 throughout the season. A recent study indicates that the ERA5 snowfall, around ∼0.3 mm day^{-1}, shows the best correspondence with satellite observations (from CloudSat) in the summer (Cabaj et al., 2020). As the JRA55 summer snowfall rate is similar to ERA5 (∼0.3 mm day^{-1}), CICE5 with JRA55-do forcing is likely to simulate smaller amount of snowfall than the satellite observations. If JRA55-do snowfall data are used, summer Arctic snowfall climatology and variations are about ∼35% and ∼20% smaller than those of JRA55.

To test the sensitivity of our model simulation results, the ocean-ice coupled model simulation is forced using atmospheric forcings (snowfall, surface air temperature, and specific humidity) from another reanalysis, MERRA2. The summer snowfall of MERRA2 is about 40% higher than JRA55 (Figure 1) and the anomalous snowfall of MERRA2 during snowstorm events are ∼15% higher than JRA55 (Figure S2 in Supporting Information S1). In this study, we replaced the snowfall of JRA55-do data set with MERRA2 snowfall to identify the impact of different snowfall forcing on sea ice during snowstorm events.

2.3.1. Historical Simulation (Hist)

We integrated our CICE5-POP2 framework with JRA55-do surface forcings (but snowfall nudged to JRA55) for 62 years from 1958 to 2019. The first 22 years (from 1958 to 1979) is used as a spin-up simulation and the remaining 40 years (from 1980 to 2019) as a historical simulation. For MERRA2 surface forcings, the initial conditions of 1980 simulated by JRA55-do surface forcings were used for the initial conditions.

Figure S3 in Supporting Information S1 shows that the majority of Arctic sea ice is covered by snow in June: CICE5 with JRA55 snowfall and CICE5 with MERRA2 snowfall consistently simulate snow depth larger than 15 cm over the Central Arctic Ocean and larger than 3 cm over the marginal ice zone. The interannual variations of June snow depth over sea ice, averaged over the entire Arctic, show a clear declining trend. In July, CICE with

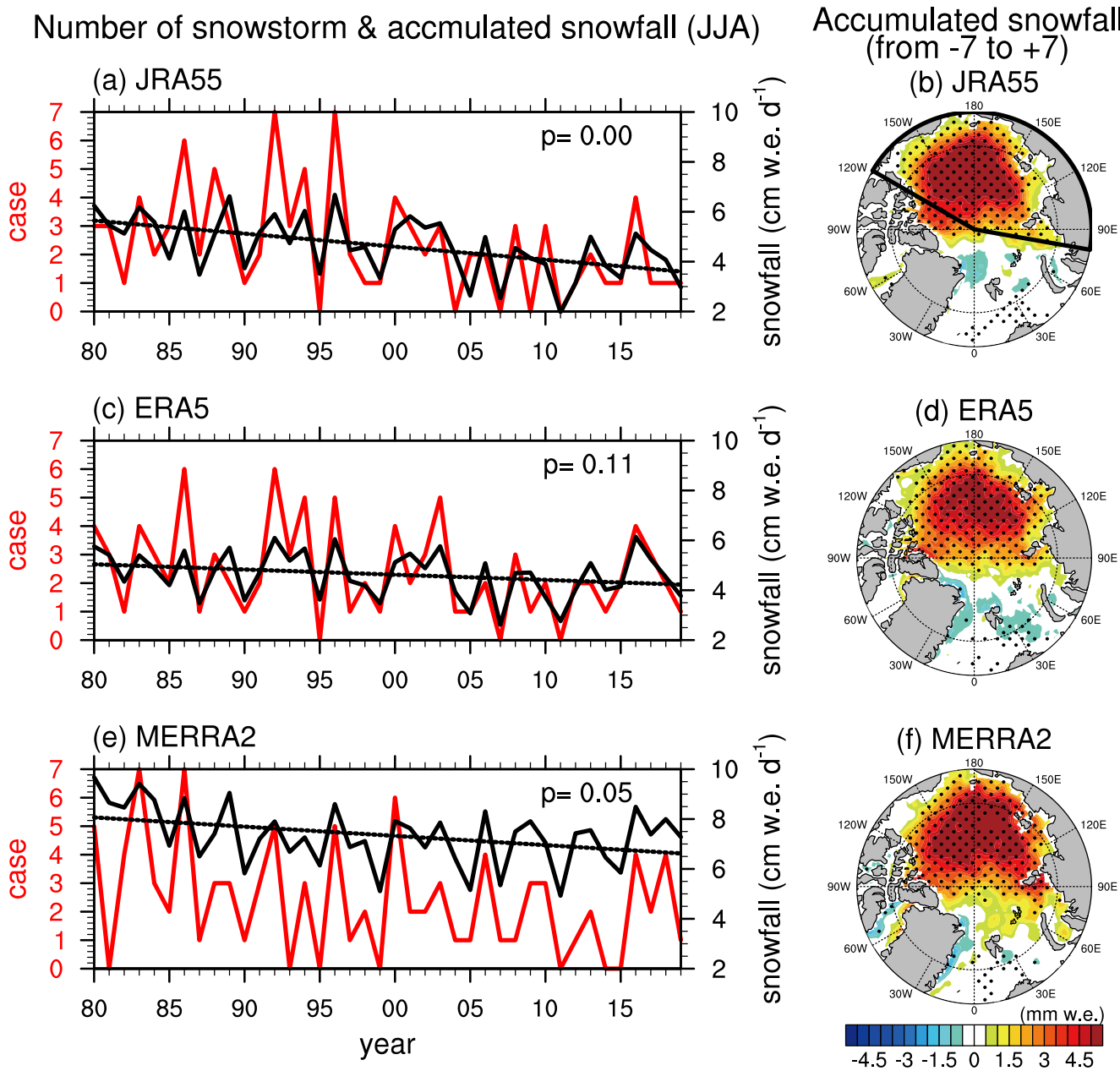

Figure 1. Interannual variations of Arctic summer snowstorms and snowfall. (Left panels (a, c, and e)) The year-to-year variations of summer (June-July-August) snowstorm frequency (red lines) and accumulated snowfall (black lines) in SWE averaged over the Eurasian-Pacific sector of the Arctic (black line in panel (b)) for (a) JRA55, (c) ERA5, and (e) MERRA2. Composite map of accumulated snowfall anomalies (in SWE) during the summer snowstorm events (from (Right panels (b, d, and f)) lag day −7 to day +7) for (b) JRA55, (d) ERA5, and (f) MERRA2. In right panel figures, statistically significant values ($p < 0.05$) are stippled.

JRA55 and MERRA2 surface forcing simulations show that snow, generally less than 5 cm, still exists over the Central Arctic Ocean (Figure S3 in Supporting Information S1).

2.3.2. Quantifying the Wind (Mechanical) Effect on Sub-Seasonal Time Scales (Figure 6)

To identify how the cyclonic wind-driven ice drifts during the summer snowstorm events impact the sea ice cover, we produce a control run from 1980 to 2019 using JRA55-do atmospheric forcing (Tsujino et al., 2018) then test the sensitivity to the associated wind anomalies, by prescribing climatological-mean 10 m wind and SLP anomalies during snowstorm events from around lag day −7 to day +7. The wind-driven mechanical effect

on sea ice can be estimated by the difference between the control simulation and the climatological-mean 10 m wind simulation.

2.3.3. Quantifying the Thermal and Mechanical Effects of Multiple Snowstorms (Figure 7)

To identify the thermal and mechanical impacts of multiple summer snowstorm events on seasonal sea ice cover, we configured another idealized simulation. From lag day −7 to day +14 of each snowstorm event, snowfall, surface air temperature, and surface specific humidity were replaced by climatological means, referred to as a "no snowstorm scenario run." The delayed post-storm date, day +14, is because preliminary testing showed that the surface air cooling signal can persist much longer than a week, as shown in Figure 4e. The *thermal effect* of summer snowstorm event on sea ice cover can be estimated by the difference between the historical run and this "no snowstorm scenario run." Similarly, the *mechanical effect* is identified by imposing *climatological-mean 10 m winds* from lay day −7 to around day +7 for each snowstorm event in CICE5. As shown in Figure 2, the low SLP anomaly during snowstorm events starts to manifest ∼1 week before the peak snowfall day, but substantially weakens ∼1 week after. The wind-driven mechanical effect on sea ice can be estimated by the difference between the historical run and the climatological-mean 10 m wind simulation.

These thermal and mechanical effects on seasonal sea ice cover are identified for each summer, from 1980 to 2019. The preceding snowstorm can affect the SIC of the subsequent snowstorms in a summer. However, the previous year's summer snowstorms cannot affect the SIC of the given simulation year.

2.3.4. Separating the Effects of Snowfall and Surface Air Cooling on Sea Ice (Figure 8)

The thermal impact can be further decomposed into the "*snowfall effect*" and "*surface air effect*." While summer Arctic snowstorm events are also accompanied by changes in rainfall and downward radiation, these anomalies are relatively small (see Table 3). The "*snowfall effect*" includes the impact on changes in albedo and also changes in surface heat capacity. The "*surface air effect*" includes the impact from changes in near-surface air temperature and humidity and their impact on turbulent heat fluxes and surface temperature. The "*snowfall effect*" can be identified by imposing *climatological-mean snowfall* from lag day −7 to day +14 during the snowstorm event(s), while other variables are given as the same historical forcings. Likewise, the "*surface air effect*" can be identified by imposing *climatological-mean 2* m *air temperature and specific humidity* during the snowstorm event(s), while other variables are given as the same historical forcings. All of our model experiments are summarized in Table 2.

3. Sea Ice Response to Summer Snowstorms

3.1. Summer Snowstorm Events

Figures 1a, 1c, and 1e (Left panel of Figure 1) show the interannual variability of accumulated snowfall (black lines) and the number of snowstorms (red lines) in summer (June-July-August), averaged over the Eurasian-Pacific sector of the Arctic (80–240°E; 69–90°N, black line of Figure 1b) for JRA55, ERA5, and MERRA2 reanalyzes. Sea ice in the Atlantic sector of the Arctic retreats early in spring and exerts less influence on summer sea ice extent and is thus excluded from this analysis. Consistent with previous studies (Barrett et al., 2020; Boisvert et al., 2018), the three reanalyzes show similar interannual variability in summer snowfall: the detrended correlation coefficient between JRA55 and ERA5 is 0.94 and between JRA55 and MERRA2 is 0.79.

Arctic summer (June-July-August) snowfall generally exhibits decreasing trends in recent decades (black lines in Figures 1a, 1c, and 1e), consistent with previous studies that suggest lower tropospheric warming has increased the fraction of precipitation falling as rain instead of snow (Bintanja & Andry, 2017; Screen & Simmonds, 2012). The declining trend in summer snowfall is statistically significant ($p < 0.05$) in JRA55 and MERRA2 but is not statistically significant in ERA5. Consistent with previous studies (Barrett et al., 2020; Boisvert et al., 2018; Cabaj et al., 2020), Arctic summer snowfall in MERRA2 is generally higher than other reanalysis products. Likewise, the numbers of snowstorm events in these three reanalyzes show similar interannual variations and long-term trends (red lines in Figures 1a, 1c, and 1e). Over the 40 years from 1980 to 2019, we identify a total of 95, 96, and 96 snowstorm events in JRA55, ERA5, and MERRA2, respectively. JRA55 and ERA5 indicate that there was no snowstorm event in 2007 summer (only one snowstorm event in MERRA2), during which observed downward shortwave radiation at the surface was exceptionally high due to reduced cloud cover (Kay et al., 2008).

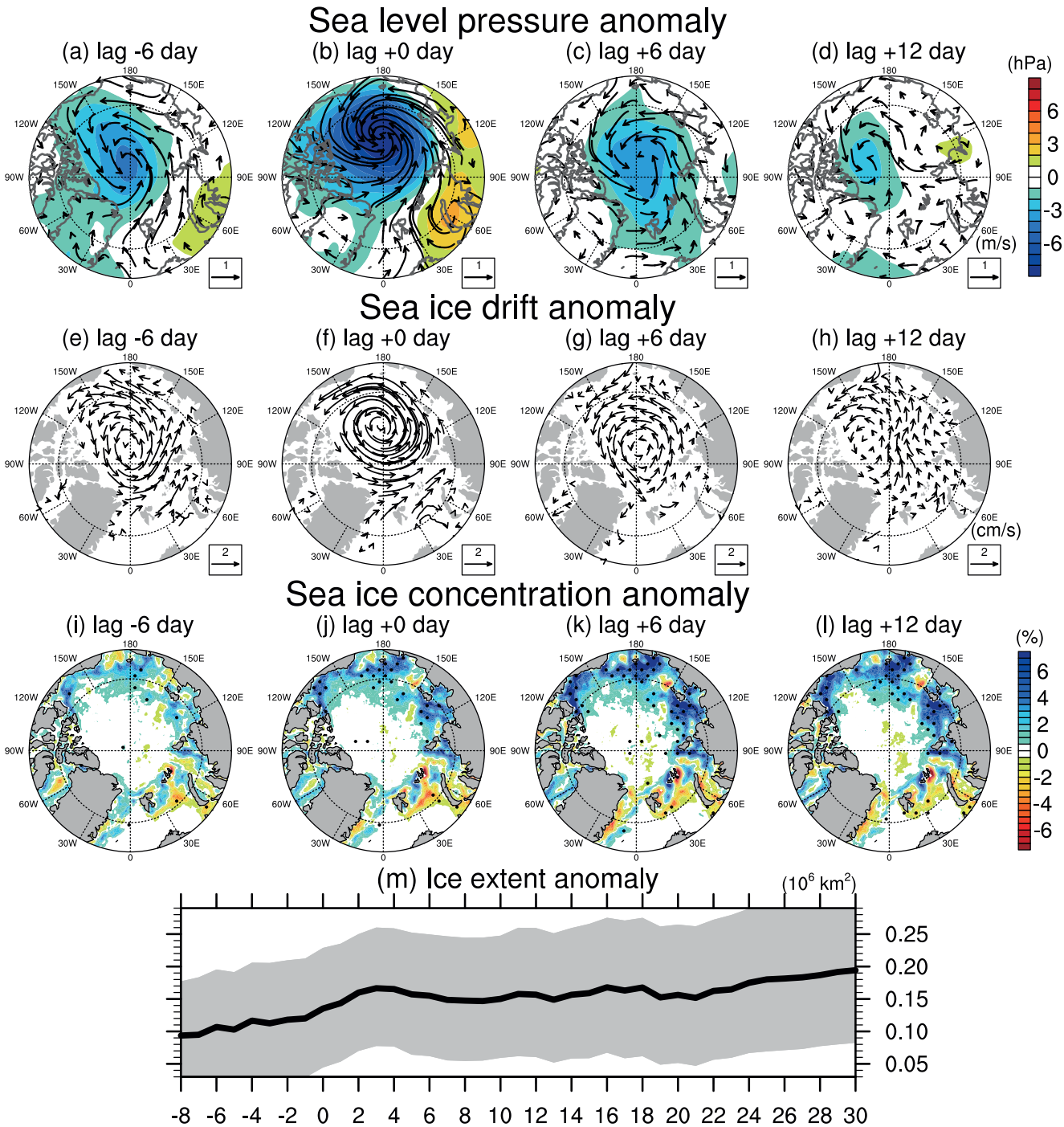

Figure 2. Observed sea ice drift and extent anomalies. The lag composite maps of anomalous (a–d) sea level pressure (hPa) with 10-m winds (m/s), (e–h) sea ice drifts (cm/s; vector), and (i–l) sea ice concentration (%) during summer (June-July-August) snowstorm events (97 cases) from 1980 to 2019, specifically for (a, e, and i) lag day −6, (b, f, and j) lag day 0, (c, g, and k) lag day +6, and (d, h, and l) lag day +12. (m) The composite Arctic sea ice extent anomaly (10^6 km^2) during and after summer snowstorm events. In (i–l), statistically significant values ($p < 0.05$) are stippled. Gray shadings in panel (m) indicate 95% intervals of the composite Arctic sea ice extent anomalies.

The composite map of accumulated snowfall anomalies during the snowstorm events, specifically from lag day −7 to day +7 shows basin-scale increase in snowfall including the Laptev, East Siberian, Chukchi, and Beaufort Seas as well as the inner Arctic Ocean (Figures 1b, 1d, and 1f). The total accumulated snowfall during these

Table 2
Summary of Model Experiments

Experiment	Forcings			
	10 m-winds	Snowfall	Surface air temperature (T)	Surface air humidity (Q)
Hist	Hist[a]	Hist	Hist	Hist
Clim_Wind	Clim−7 + 7[b]	Hist	Hist	Hist
Clim_Snow + T + Q	Hist	Clim−7 + 14[c]	Clim−7 + 14	Clim−7 + 14
Clim_Snow	Hist	Clim−7 + 14	Hist	Hist
Clim_T + Q	Hist	Hist	Clim−7 + 14	Clim−7 + 14

[a]Hist is historical forcing. [b]Clim−7 + 7 is climatological forcing from lag day −7 to 7. [c]Clim−7 + 14 is climatological forcing from lag day −7 to 14.

Note. Mechanical effect: Hist—Clim_Wind, Thermal effect: Hist—Clim_Snow + T + Q, Snowfall effect: Hist—Clim_Snow, Surface air cooling/drying effect: Hist—Clim_T + Q.

snowstorm events are 104, 100, and 151 cm of snow water equivalent for JRA55, ERA5, and MERRA2, respectively, accounting for ∼56%, 54%, and 51% of the total summer snowfall, respectively.

3.2. Observed Response of Sea Ice to Summer Snowstorms

As discussed in Webster et al. (2019), snowstorms are associated with the development of synoptic-scale low pressure cyclones. The composite maps of summer SLP anomalies show that a low pressure system starts to develop around a week before the peak snowfall day (Figure 2a). During the snowfall peak, SLP anomalies in the center of the cyclones are about 6–7 hPa lower than average (Figure 2b). These low-pressure anomalies rapidly weaken ∼1 week after the peak (Figure 2c). Satellite-derived sea ice drift vectors (M. A. Tschudi et al., 2019) show that the development of low pressure is accompanied by a cyclonic ice drift circulation pattern, which can persist for 1–2 weeks (Figures 2e–2h). During the snowstorm peak, at lag day 0, strong south-westerlies (north-eastward wind stress) over the Chukchi–Beaufort Seas (Figure 2b) are accompanied by anomalously strong eastward ice drifts (Figure 2f) because the ice velocity is angled to the right of the wind velocity by around 20–40° in Arctic summer (Park & Stewart, 2016). The cyclonic ice drifts weaken the transpolar transport of ice from the Chukchi Sea to the Fram Strait (Figure 2f), which has previously been highlighted as a possible contributor to positive summer ice extent anomalies (Schreiber & Serreze, 2020; Screen et al., 2011).

Our lagged composite map shows that SIC gradually increases by more than 5% over wide areas of the Arctic including the Kara, Laptev, East Siberian, Chukchi, and Beaufort Seas (Figures 2i–2l) after the snowstorm peak. Arctic sea ice extent continuously increases even 30 days after the snowstorm peak (Figure 2m), although internal variability is superimposed on this trend (gray shadings in Figure 2m). From lag −8 day to +30 day, sea ice extent increases by about 0.1×10^6 km^2, which is ∼0.34 standard deviations of the (detrended) interannual variability in summer Arctic sea ice extent. The reanalyzes suggest between 2 and 3 snowstorms occur on average each summer. The impacts of multiple snowstorms on seasonal Arctic sea ice cover are investigated using the ocean-sea ice model in Section 4.2.

3.3. Observed Response of Surface Heat Fluxes Over Sea Ice

As shown in a recent observational study (Perovich et al., 2017), summer snowstorms can be accompanied by changes in surface albedo and turbulent heat fluxes, which can affect sea ice cover on seasonal time scales. Net surface heat flux over snow can be written as:

$$Q_{\text{net}} = -\text{SW}^{\downarrow}(1-\boldsymbol{\alpha}) + \left(\text{LW}^{\uparrow} - \text{LW}^{\downarrow}\right) + \left(\text{SHF}^{\uparrow} + \text{LHF}^{\uparrow}\right) + C + R, \quad (1)$$

where $\text{SW}^{\downarrow}$ is downward shortwave radiation and $\boldsymbol{\alpha}$ is surface albedo. $\text{LW}^{\downarrow}$ and $\text{LW}^{\uparrow}$ imply downward and upward surface longwave radiations, respectively (e.g., Dou et al., 2019; Parkinson & Washington, 1979; Wu et al., 1999). $\text{SHF}^{\uparrow}$ and $\text{LHF}^{\uparrow}$ denote surface sensible and LHFs, respectively. Downward surface heat flux implies negative Q_{net} and upward surface heat flux implies positive Q_{net}. In Arctic summer, Q_{net} is generally negative because of strong

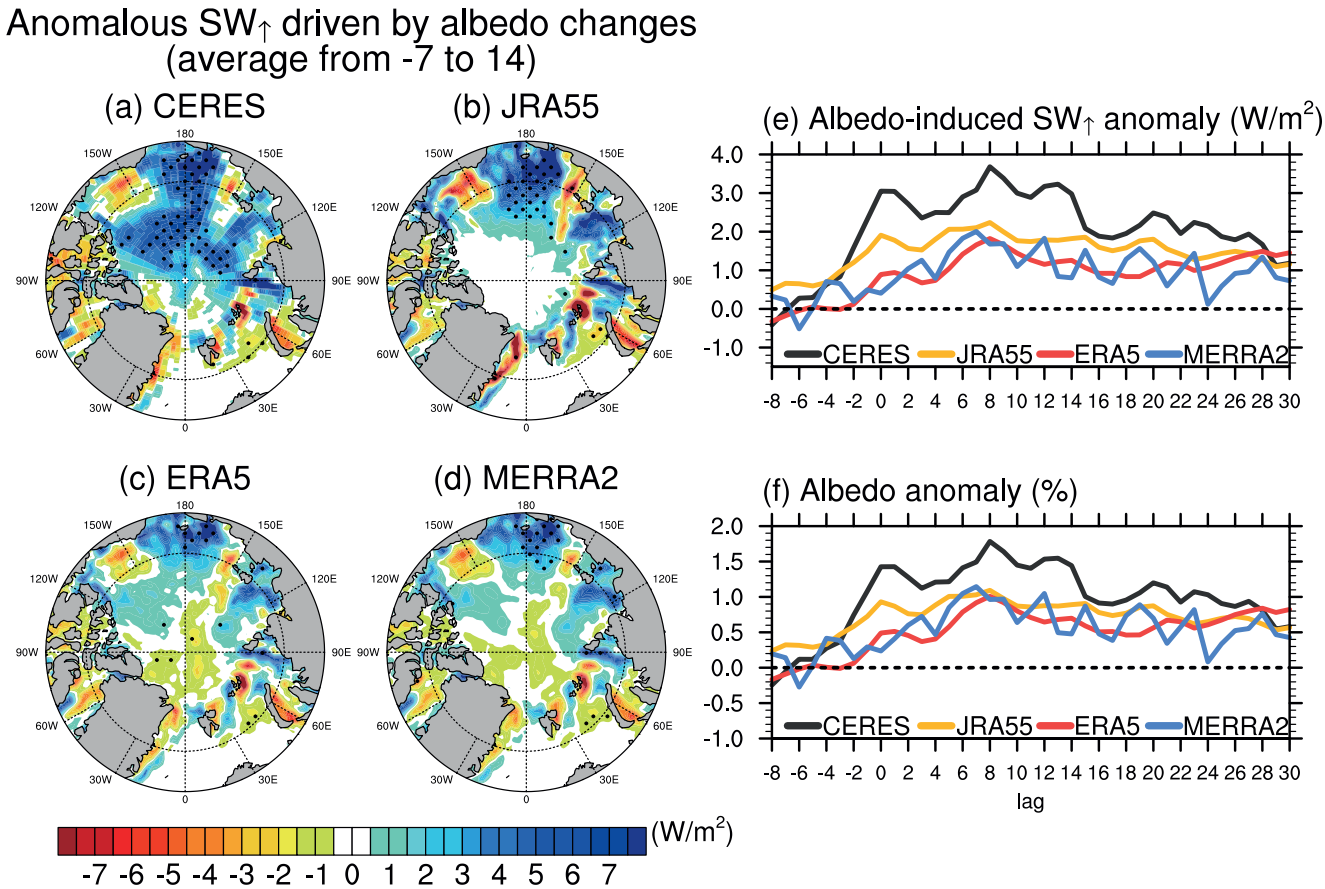

Figure 3. Observed upward shortwave radiation and surface albedo anomalies. (Left panels (a–d)) Composite maps of anomalous upward shortwave radiation driven by albedo changes (W m^{-2}) during/after summer snowstorm events, averaged from lag day −7 to day +14 for (a) Clouds and the Earth's Radiant Energy System (CERES), (b) JRA55, (c) ERA5, and (d) MERRA2. (Right panel) The lagged composites of (e) anomalous upward shortwave radiation driven by albedo changes (W m^{-2}) and (f) albedo anomaly (%) averaged over the Eurasian-Pacific sector of the Arctic for CERES (black), JRA55 (orange), ERA5 (red), and MERRA2 (blue) during/after snowstorm events. In (a–d), statistically significant values ($p < 0.05$) are stippled.

sunlight ($SW^{\downarrow}$). C is the conductive heat flux from the top of ice to snow surface, and R is the heat input by rain. We cannot calculate C (conductive heat flux) directly from observations. We can also express Equation 1 as the contributions to changes in the surface heat flux:

$$\Delta Q_{\text{net}} = -(1-\boldsymbol{\alpha})\Delta \text{SW}^{\downarrow} + \text{SW}^{\downarrow}\Delta\boldsymbol{\alpha} + \Delta\left(\text{LW}^{\uparrow} - \text{LW}^{\downarrow}\right) + \Delta\left(\text{SHF}^{\uparrow} + \text{LHF}^{\uparrow}\right) + \Delta C + \Delta R \quad (2)$$

3.3.1. Surface Albedo

How does surface albedo change ($\Delta\boldsymbol{\alpha}$) during/after snowstorm events? JRA55, ERA5, and MERRA2 show consistent increase in surface albedo (Figures 3b–3d), although show little change in albedo within the Central Arctic Ocean where perennial sea ice is dominant and where the wind-driven SIC response is small (Figures 2i–2l). Satellite-derived estimates of surface albedo from CERES (Doelling et al., 2013) shows albedo-induced increases in upward shortwave radiation ($-\text{SW}^{\downarrow}\Delta\boldsymbol{\alpha}$) of up to ~8 W m^{-2} over wide regions of the Arctic Ocean including the Central Arctic (Figure 3a). The albedo anomalies averaged over the Eurasian-Pacific sector of the Arctic indicate that the albedo responses in the reanalyzes are weaker than CERES (Figures 3e and 3f): the albedo anomaly increases by up to ~2% of the climatological albedo in CERES, whereas it is generally around 1%–1.5% in JRA55, ERA5, and MERRA2. The CERES data alludes to the direct importance of summer snowfall, and not associated sea ice drift/concentration-driven changes, on albedo increases within the consolidated Central Arctic Ocean, where sea ice cover persists until late summer.

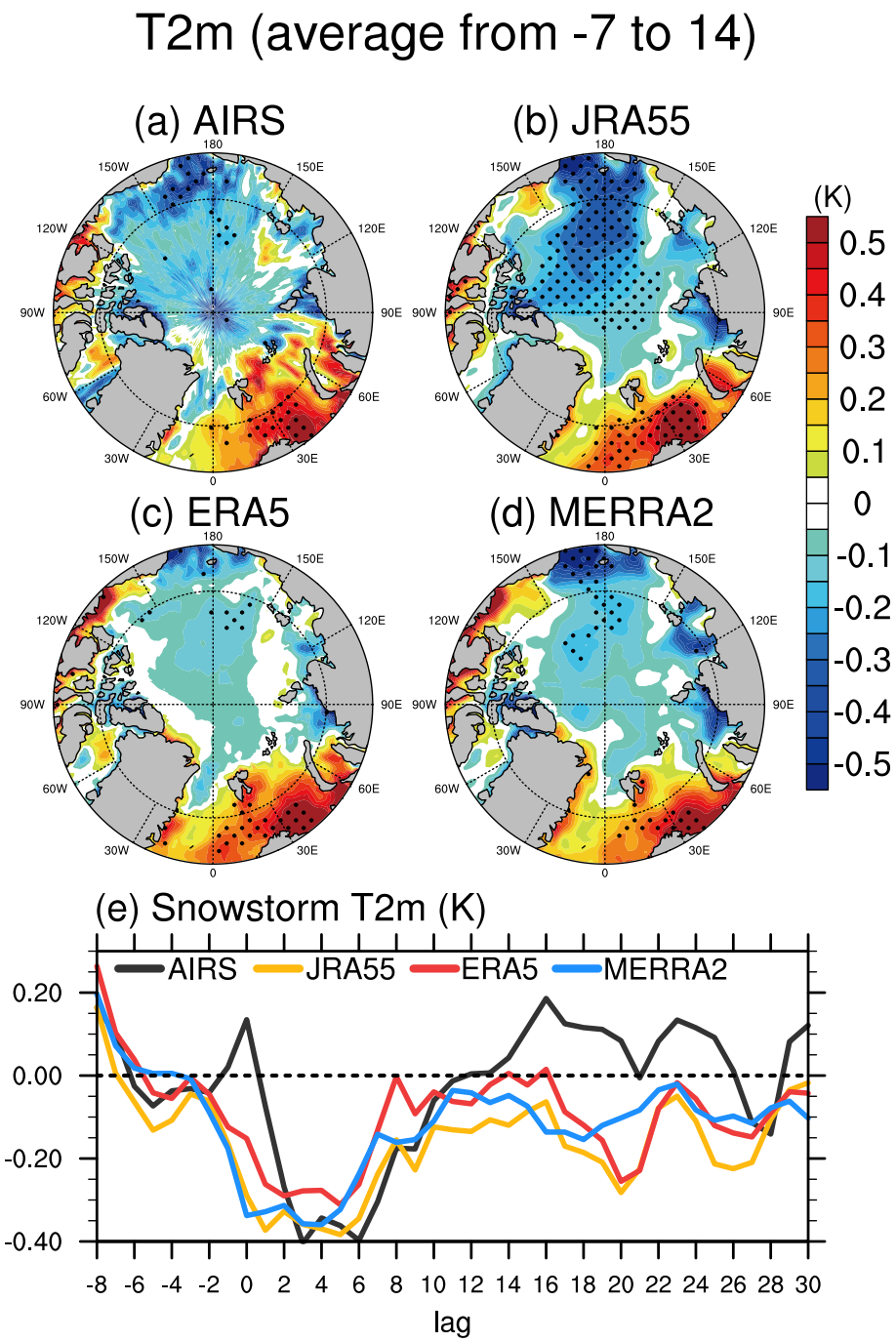

Figure 4. Observed surface air temperature anomalies. (a–d) Composite maps of surface air temperatures (K) during/after summer snowstorm events, averaged from lag day −7 to day +14 for (a) Atmospheric Infrared Sounder on NASA's Aqua satellite (AIRS), (b) JRA55, (c) ERA5, and (d) MERRA2. (e) The lagged composites of surface air temperature (K) averaged over the Eurasian-Pacific sector of the Arctic for AIRS (black), JRA55 (orange), ERA5 (red), and MERRA2 (blue) during/after snowstorm events. In (a–d), statistically significant values ($p < 0.05$) are stippled.

The notable difference in surface albedo response between the observation and reanalysis data is probably due to the simplistic representation of sea ice albedo in reanalysis products. In JRA55, sea ice surface albedo is calculated as a function of solar zenith angle, skin temperature, and SIC (Kobayashi et al., 2015). In ERA5 and MERRA2, climatological mean, seasonally varying sea ice albedo is prescribed as a function of SIC. In ERA5, the surface albedo climatology is estimated from surface types (dry snow, melting snow, bare ice, meltwater

pond, open water) (Ebert & Curry, 1993), whereas the surface albedo climatology of MERRA2 was estimated from the flux tower measurements collected during the Surface Heat Budget of the Arctic Ocean experiment (Duynkerke & de Roode, 2001; Koster et al., 2015). Although the magnitudes of the albedo response are different between CERES and these reanalyzes, they exhibit similar temporal variations. Because the cyclonic wind-driven ice drift increases sea ice extent and snowfall is generally initiated a week before the snowfall peak (lag day 0), the areal-averaged surface albedo rapidly increases around lag day −6. The albedo anomaly peaks at lag day +6 and the increased albedo anomaly persists for more than lag +20 day (Figure 3f).

A ∼1%–2% increase in surface albedo in CERES and reanalysis data (Figure 3f) can have a nontrivial influence on the surface energy balance and sea ice response. In the Arctic summer, the climatological-mean downward shortwave radiation to the surface ($SW^{\downarrow}$) is around 200 W m^{-2} in CERES. Therefore, a 1% increase in surface albedo ($\Delta\boldsymbol{\alpha} = 0.01$) can reduce surface shortwave absorption by around 2 W m^{-2}. Due to the different albedo responses, the increase in shortwave radiation is around 2–3.5 W m^{-2} in CERES and 1–2 W m^{-2} in the three reanalysis products which generally persists for over a month (Figures 3e and 3f).

3.3.2. Surface Air Temperature and Turbulent Heat Fluxes

The surface albedo response from snowstorms is accompanied by similarly persistent surface air cooling (Figure 4). Satellite-observed surface air temperature, specifically AIRS (Aumann et al., 2003) and the three reanalysis products (Figures 4a–4d) show that surface air temperatures decrease over almost the entire Arctic Ocean. Surface air temperature anomalies averaged over the Eurasian-Pacific sector of the Arctic start show a rapid cooling during the onset of snowstorm, approximately a week before the peak snowfall when snowfall rapidly accumulates (Figure 4e). The negative surface air temperature anomalies persist after the snowstorms, until around lag day +10 in the AIRS observations and lag day +14 in the reanalyzes. A closer examination reveals that the surface air cooling is strongest in JRA55. In JRA55, the statistically significant cooling occurs over wide areas of the Arctic, whereas the surface air cooling is somewhat concentrated over the Chukchi Sea in AIRS, ERA5, and MERRA2 (Figures 4a–4d).

Because snowstorms are often accompanied by wind strengthening (Figures 2a–2c), the combined effect of winds and surface air cooling can increase surface turbulent heat fluxes. Indeed, the three reanalyzes consistently indicate that the upward turbulent heat flux increases in the basin-wide Arctic Ocean during/after the snowstorm (Figure 5). The upward turbulent heat flux averaged over the Eurasian-Pacific increases from lag day −6 and positive anomalies persists until around day +10. The increase of turbulent heat flux is particularly large in JRA55 up to ∼4 W m^{-2}, which is twice larger than the increases in ERA5 and MERRA2. The ∼4 W m^{-2} increase in turbulent heat flux during the peak of snowstorms in JRA55 is larger than the increased albedo effect in JRA55 (orange line in Figure 3e), although the albedo anomaly persists for longer.

3.3.3. Downward Shortwave and Longwave Radiations

In CERES, downward shortwave radiation $\Delta SW^{\downarrow}$ reduces during snowstorm events by up to ∼3 W m^{-2}, contributing to delayed snow melt (Figure S4 in Supporting Information S1). However, the composite time series further show that $\Delta SW^{\downarrow}$ rebounds after snowstorm events: $\Delta SW^{\downarrow}$ averaged from lag day −7 to +14 (during and after snowstorm events) is within ∼0.3 W m^{-2}. Downward longwave radiation ($LW^{\downarrow}$) increases by up to ∼0.5 W m^{-2}, mainly over the Beaufort Sea, during the peak of the snowstorms, but rapidly reduces towards climatology (Figure S4 in Supporting Information S1). Downward shortwave and longwave radiation anomalies, averaged over the Eurasian-Pacific sector of the Arctic from lag day −7 to +14, are generally lower than other surface heat flux terms such as the albedo-induced upward shortwave radiation anomaly (see Table 3).

3.3.4. Other Effects (Rainfall and Snow Cold Content)

Unlike snowfall, which rapidly accumulates during snowstorm events, rainfall does not change much: slightly increasing over the more marginal Arctic and decreasing over the Central Arctic (Figure S2 in Supporting Information S1). During the snowstorm peak, rainfall increases by around 0.15 mm. Assuming that rain temperature is close to surface air temperature, the associated ΔR is relatively small, within ∼0.3 W m^{-2} (Table 3). Newly fallen snowfall can also act as an energy sink as it takes energy to increase snow temperature to its melting temperature, which is referred to as cold content: $M_i = C_i\,\rho_s h_s T_s$, where C_i is the specific heat of ice (2.1×10^3 J kg^{-1} $°C^{-1}$), ρ_s

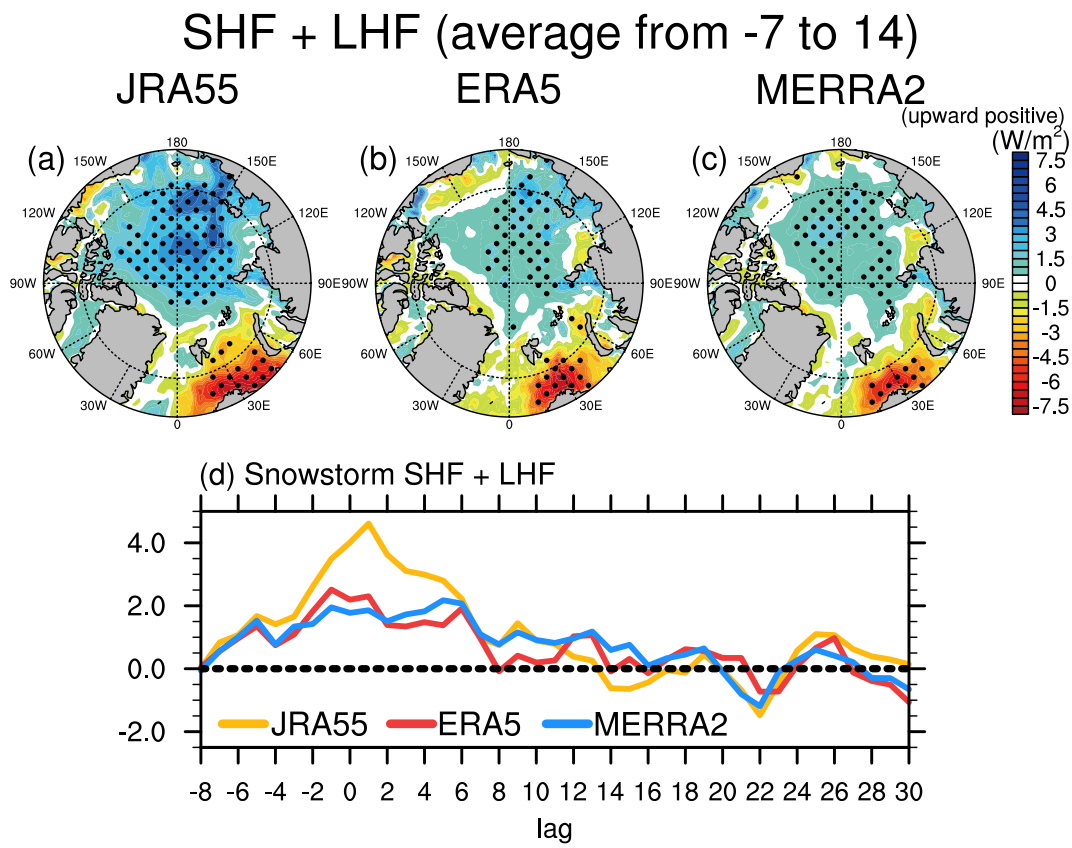

Figure 5. Observed surface turbulent heat flux anomalies. (a–c) Composite maps of surface turbulent heat fluxes, the sum of sensible and latent heat fluxes (W m^{-2}), during/after summer snowstorm events averaged from lag day −7 to day +14 for (a) JRA55, (b) ERA5, and (c) MERRA2. (d) The lagged composites of surface turbulent heat fluxes averaged over the Eurasia-Pacific sector of the Arctic for JRA55 (orange), ERA5 (red), and MERRA2 (blue) during/after snowstorm events. In (a–c), statistically significant values ($p < 0.05$) are stippled.

is the snow density, h_s the snow depth, and T_s (°C) the snow temperature. Net surface heat flux is about 40 W m^{-2} downward in summer (Uttal et al., 2002), implying that warming ~10 cm of snow to melting point can happen within an hour, even if the snowfall temperature is assumed to be as low as −4°C.

4. Model Simulated Mechanical and Thermal Impacts on Sea Ice

4.1. Wind-Driven Mechanical Impact (on Sub-Seasonal Time Scales)

Our observational analysis suggests that a single summer snowstorm event is accompanied by a positive sea ice extent anomaly of around 0.12×10^6 km^2 (Figure 2m). Here, we seek to identify the specific processes driving this increase on sub-seasonal time scales. The wind-driven mechanical effect on sea ice can be estimated by the difference between the historical simulation and the climatological-mean 10 m wind simulation (see Section 2 for details). Our model experiments show that the cyclonic wind forcing (Figures 2a–2d) during the summer snowstorm events drives the cyclonic sea ice drifts (Figures 6a–6d). This is consistent with satellite-derived ice drift anomalies (Figures 2e–2h), although model-simulated ice drift speed anomalies are generally higher than the satellite observations, especially in lag day +6 and +12. Both the satellite observations and model simulations show that Arctic summer snowstorms are associated with eastward ice drifts from the Beaufort Sea to the Central Arctic (Figures 2f and 6b). Our CICE5 simulations show that cyclonic sea ice drifts also decrease SIC in the Central Arctic Ocean while increasing SIC in the Eastern Arctic Ocean, including the Chukchi and East Siberian Seas (Figures 6e–6h) due to the divergent ice flux.

A close examination of Figure 6 indicates that the ice flux divergence (red colors in Figure 6f) is somewhat more pronounced east of the international date line (e.g., within the Beaufort Sea) than west of the date line. This

Table 3
The Surface Heat Flux Anomaly of Each Term in Equation 2

Name of each surface heat flux term	Equation of each surface heat flux term	The energy flux averaged from day −7 to +14	Time periods for climatological means
Downward shortwave radiation	$-(1-\alpha)\Delta SW^{\downarrow}$	**CERES: 0.27 W/m²**	2000–2019
Downward longwave radiation	$-\Delta LW^{\downarrow}$	**CERES: −0.07 W/m²**	2000–2019
Albedo-induced upward shortwave radiation	$SW^{\downarrow}\Delta\alpha$	**CERES: 2.3 W/m²**	2000–2019
Turbulent heat flux (SHF + LHF)	$\Delta(SHF^{\uparrow}+LHF^{\uparrow})$	No observation	2000–2019
		Reanalyzes average: 1.44 W/m²	
Heat input by rain	ΔR	No observation	2000–2019
		Reanalyzes average: −0.3 W/m²	

Note. $\Delta Q_{net} = -(1-\alpha)\Delta SW^{\downarrow} + SW^{\downarrow}\Delta\alpha + \Delta\left(LW^{\uparrow} - LW^{\downarrow}\right) + \Delta(SHF^{\uparrow} + LHF^{\uparrow}) + \Delta C + \Delta R$.

is consistent with a recent study that sea ice decreases to the east of Arctic cyclones and increases to the west (Clancy et al., 2022). However, the wind-driven sea ice flux divergence pattern varies widely on a case-by-case because the response of summer Arctic sea ice cover is highly sensitive to the timing and location of a cyclone relative to the sea ice edge (Lukovich et al., 2021). Our model-simulated ice flux divergence pattern shown in Figure 6 is an average response of more than 90 summer snowstorm cases.

The lagged composite of sea ice extent anomalies shows a continuous increase in sea ice extent during and after snowstorm events, approximately by 0.08×10^6 km^2 from lag −8 day to +30 day (black line in Figure 6i). Our model simulation underestimates the expansion of sea ice extent shown in the satellite observations, which is around 0.12×10^6 km^2 from lag −8 day to +30 day (compare black lines in Figures 2m and 6i). The sea ice extent anomalies driven by the idealized model experiment with the surface wind anomaly forcing (blue line in Figure 6i) compare well to the snowstorm events composite (black line in Figure 6i) from lag day −8 to around day +14, suggesting that the initial expansion of sea ice extent during the summer snowstorm events is almost entirely driven by the cyclonic wind-driven ice drifts. However, the impact of wind-driven ice drifts on the expansion of sea ice extent is limited to around 2 weeks after the snowstorm peak (lag day +14): sea ice extent anomaly continuously increases from lag day −8 to around +13, but then continuously decreases (blue line in Figure 6i). There is a large difference in sea ice extent anomalies between the historical simulation (black line in Figure 6i) and the wind effect during the summer snowstorm events at lag day +30. Our model results suggest that the associated summer snowstorm cyclonic sea ice drift may provide significant sea ice extent impacts on daily and weekly time-scales but is probably not a key factor in understanding the seasonal sea ice extent response.

4.2. Thermal and Mechanical Impacts (on Seasonal Time Scales)

Because multiple snowstorm events generally occur in a given summer (Figures 1a, 1c, and 1e), we seek an assessment of the impact of multiple summer snowstorms on seasonal Arctic sea ice extent using CICE5. To explore the sensitivity of sea ice extent to the net effect of multiple snowstorm events in a given summer, we performed idealized perturbation experiments for all the summer snowstorm events detected over our study period (Figures 1a, 1c, and 1e). To identify the snowfall-induced *thermal effect*, *climatological-mean snowfall*, *surface air temperature*, *and surface specific humidity* during the snowstorm event(s) are imposed in CICE5 (see Section 2 for details). The thermal impact of summer snowstorms in a summer can then be estimated from the difference between the historical simulation and the snowstorm-removed historical simulation. Likewise, the *mechanical effect* is identified by imposing *climatological-mean 10* m *winds* for each snowstorm event in CICE5. These thermal and mechanical effects on *seasonal* Arctic sea ice cover are identified for each summer, from 1980 to 2019.

4.2.1. Thermal Effect

Our CICE5 with JRA55 surface forcing simulations show that the snowfall-induced thermal effect (combination of increased surface albedo and surface air cooling) on the expansion of Arctic sea ice extent is relatively small until mid-July, generally within 0.05×10^6 km^2, but rapidly increases from late July and peaks in early September

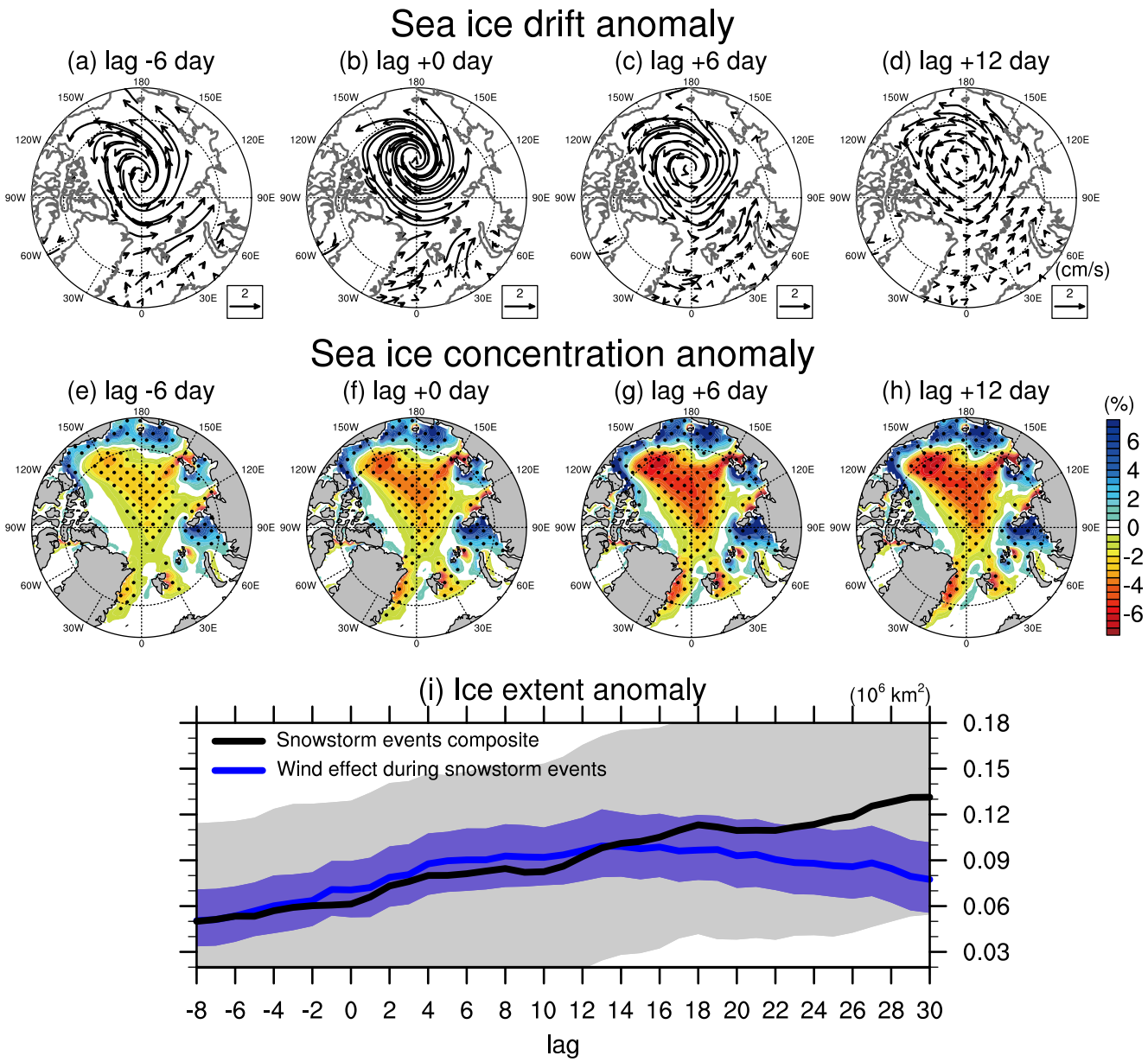

Figure 6. Wind-driven ice drift and extent anomalies simulated by CICE5. The CICE response of wind forcing to lag composite map of (a–d) sea ice drift anomalies (cm/s; vector) and (e–h) sea ice concentration anomaly (%) during/after summer snowstorm events (95 cases) from 1980 to 2019, specifically for (a and e) lag day −6, (b and f) lag day 0, (c and g) lag day +6, and (d and h) lag day +12. (i) The CICE-simulated Arctic sea ice extent anomaly (10^6 km^2) driven by anomalous winds (blue line) and by all forcings (black line) during/after summer snowstorm. In (e–h), statistically significant values ($p < 0.05$) are stippled. Gray shadings in panel (i) indicate 95% intervals of composite Arctic sea ice extent anomalies driven by all forcings (gray) and by the anomalous winds (blue).

(Figure 7a). Because sunlight is strongest from late-June to early-July, fresh snowfall and the associated albedo effect is likely to be strongest in July. However, the climatological-mean SICs over the Central Arctic Ocean are still close to 100% until mid-July and the response is confined to the marginal ice zone (Figure 7b). As Arctic sea ice rapidly retreats in late July and the marginal ice zone expands into the Central Arctic Ocean, the thermal effect on SIC emerges clearly. SIC anomalies in August and September show basin-wide increases in sea ice cover of over 10% (Figures 7c and 7d), highlighting the thermal impact of the snowstorms in damping summer sea ice extent decline. The thermal impact on Arctic sea ice extent is greatest in early September, during which the positive sea ice extent anomaly increases to ~0.2×10^6 km^2 on average, which is approximately 0.4 standard deviations of the August-September (detrended) interannual Arctic sea ice extent variability.

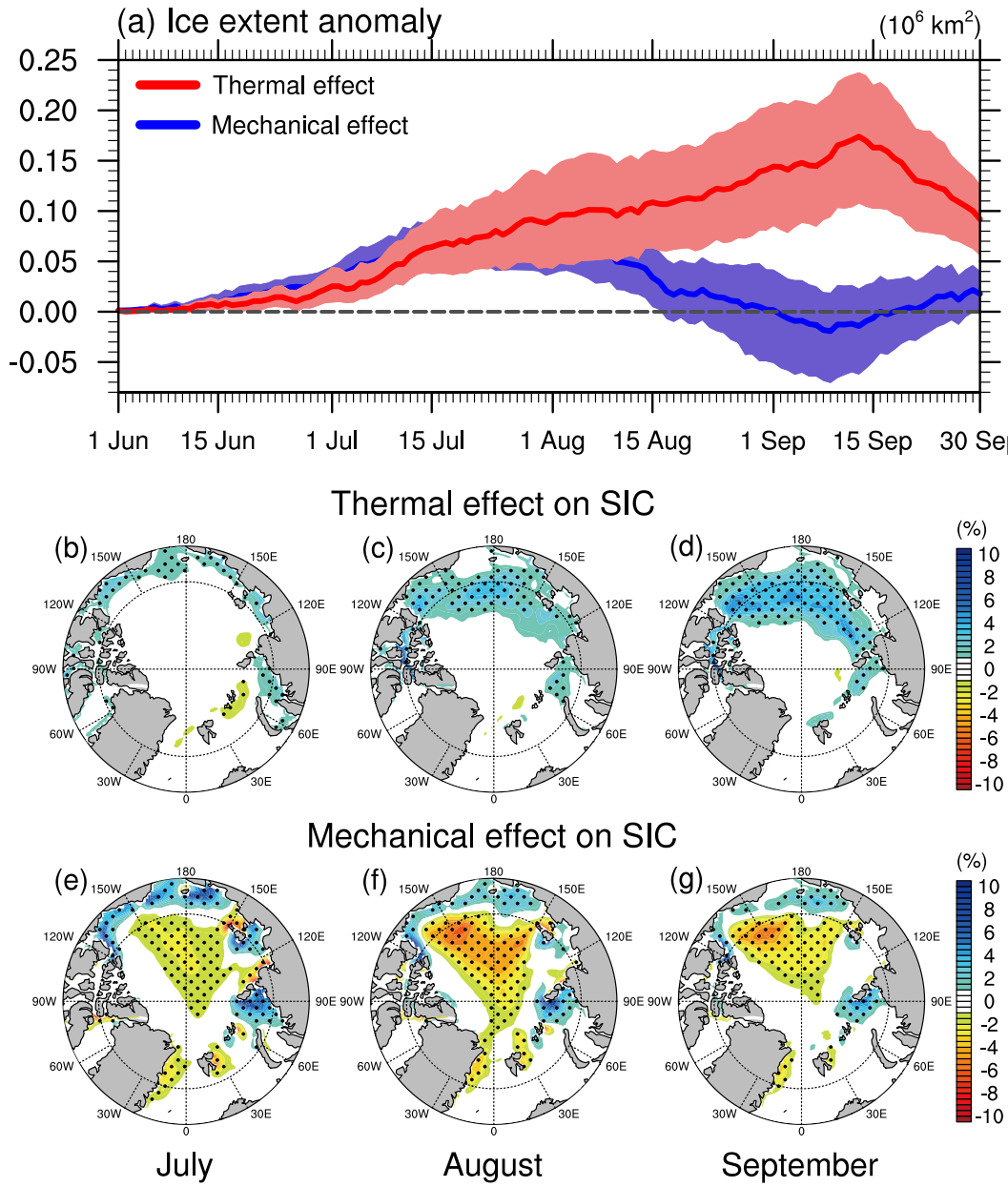

Figure 7. Thermal and mechanical impacts of snowstorms on seasonal sea ice cover simulated by CICE5. The composite means of (a) seasonal sea ice extent anomalies (10^6 km^2) driven the thermal effect of snowfall (red line) and wind-induced mechanical effect (blue line), and (b–g) sea ice concentration anomalies (%) driven by (b–d) thermal and (e–g) mechanical effects in (b and e) July, (c and f) August, and (d and g) September. These are composite anomalies of all the summer snowstorm events from 1980 to 2019 simulated by CICE—JRA55 forcing. Shadings in panel (a) indicate 95% intervals of composite anomalies. In (b–g), statistically significant values ($p < 0.05$) are stippled.

4.2.2. Mechanical Effect

Unlike the thermal effects that peak in late summer, the wind-driven mechanical effect on the expansion of sea ice extent is greatest in July, which is comparable to the thermal effect during this period (Figure 7a). Consistent with Figure 6, the cyclonic wind-driven ice flux divergence decreases SIC in the Central Arctic Ocean but increases SIC along the marginal ice zone in July and August (Figures 7e and 7f). The mechanical effect gradually weakens in August (Figure 7f) and slightly decreases sea ice extent anomaly in September (Figure 7a) when only the perennial sea ice remains. On seasonal time scales, the thermal effect of snowstorms on Arctic sea ice extent is

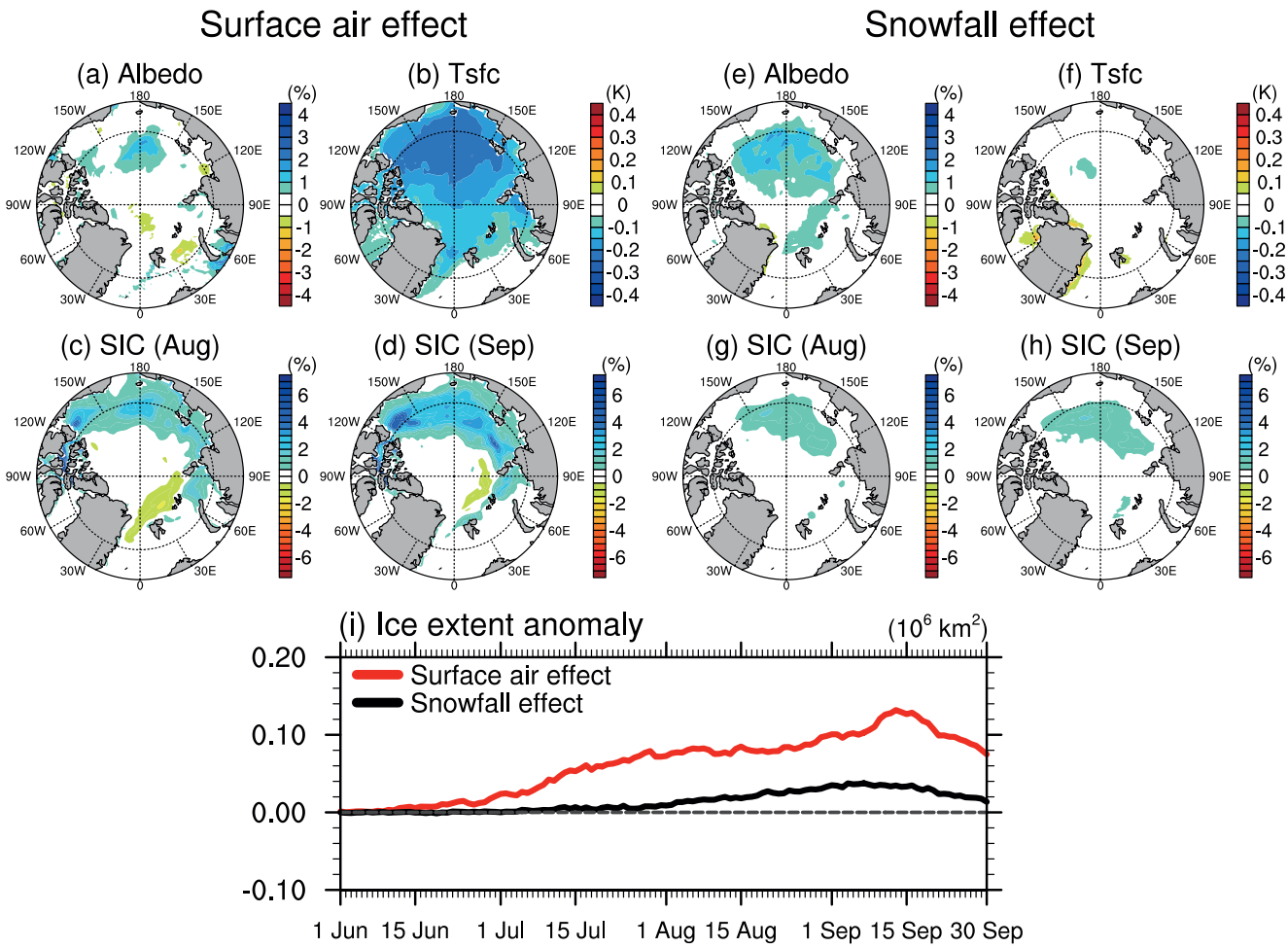

Figure 8. Surface air versus snowfall effects on summer sea ice simulated by CICE5. The composite means of (a and e) albedo (%), (b and f) surface temperature (K), and (c and g) August, (d and h) September sea ice concentration anomalies (%) during/after summer snowstorm events averaged from lag day −7 to day +14, driven by (Left panel (a–d)) surface air and (Right panels (e–h)) snowfall. (Bottom panel (i)) The composite means of seasonal sea ice extent anomalies (10^6 km^2) driven by surface air (red line) and snowfall (black line). These are composite anomalies of all the summer snowstorm events from 1980 to 2019 simulated by CICE5—JRA55 forcing.

larger than the mechanical effect and contributes significantly to the interannual variability in late summer Arctic sea ice extent.

The wind effect not only changes sea ice drift but also changes surface sensible and LHFs. However, the increased surface turbulent heat fluxes during/after the snowstorm events are mostly driven by surface air cooling/drying. The wind strengthening alone has little influence on surface turbulent heat flux because the climatological-mean air-sea temperature differences are generally small in Arctic summer.

4.3. Separating the Snowfall Versus Surface Air Effects on Seasonal Sea Ice

The thermal impact can be further decomposed into a "*snowfall effect*" and "*surface air effect*." Surface air temperature strongly covaries with surface specific humidity, keeping the surface relative humidity and the associated snow sublimation almost unchanged (Lim et al., 2022). The "*snowfall effect*" can be identified by imposing *climatological-mean snowfall*, whereas the "*surface air effect*" can be identified by imposing *climatological-mean* 2 m *air temperature and specific humidity* during snowstorm events from lag day −7 to day +14 (see Section 2 for details).

Our CICE5 simulations show that the snowfall effect and the surface air cooling effect explain about 25% and 75% of the thermal effect–induced summer sea ice extent anomalies, respectively (Figure 8i). As expected,

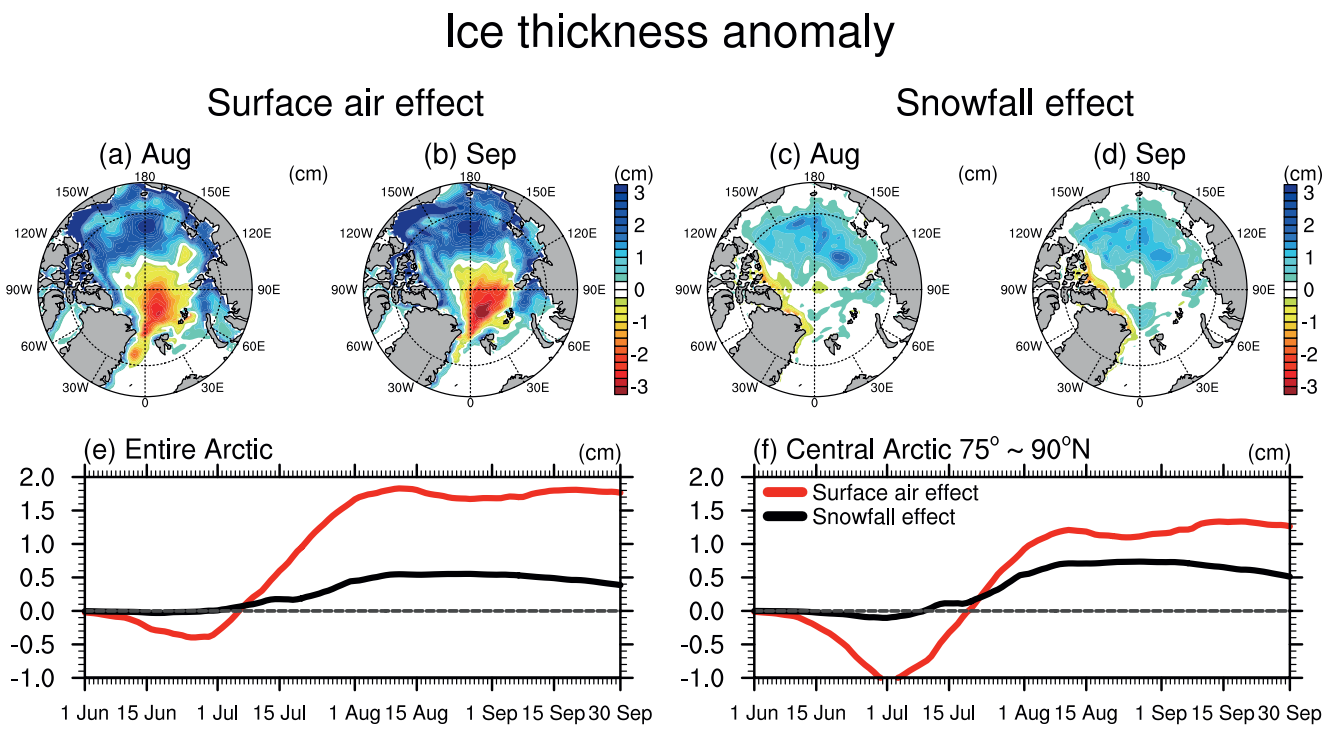

Figure 9. Surface air versus snowfall effects on summer sea ice thickness simulated by CICE5. The composite means of (a and c) August and (b and d) September sea ice thickness anomalies (cm) during/after summer snowstorm events averaged from lag day −7 to day +14, driven by (a and b) surface air and (c and d) snowfall. The composite means of seasonal sea ice thickness anomalies (cm) driven by surface air (red line) and snowfall (black line) for (e) entire Arctic and (f) central Arctic. These are composite anomalies of all the summer snowstorm events from 1980 to 2019 simulated by CICE5—JRA55 forcing.

snowfall can effectively increase albedo (Figure 8e) but has little influence on surface temperature (Figure 8f). The decrease in surface temperature is mostly associated with the surface air effect (Figure 8b). This implies that surface air cooling is far more effective in changing conductive heat flux and dampening sea ice loss than snowfall in our CICE5 simulations. A decrease in surface temperature during snowstorm events can increase the conductive heat flux ($\Delta C > 0$), which contributes to dampened summer sea ice loss by increasing ΔQ_{net} in Equation 2. However, because surface air cooling of JRA55 is larger than the AIRS observations and other reanalyzes during summer snowstorm events (Figure 4), the surface air effect is likely to be overestimated in our simulations. Furthermore, snow microstructure is highly simplified as a constant spherical shape in CICE5 (Briegleb & Light, 2007). Although snow crystal with non-spherical shape has a higher albedo and freshly fallen snow has sharp non-spherical curvatures (Jin et al., 2008), CICE5 assumes a constant spherical shape. Therefore, the snow albedo effect of freshly fallen snow is potentially underestimated in CICE5 because of the simple snow grain radius and shape.

While most of our study is focused on SIC and extent, our CICE5–simulated sea ice thickness anomalies also show that the surface air effect can have a nontrivial impact on sea ice thickness over wide areas of the Arctic (Figure 9), with the surface air effect again greater than the snowfall effect. However, over the Central Arctic Ocean, latitudes higher than 75°N, the impact of snowfall on sea ice thickness is comparable to that of surface air cooling/drying (Figure 9f).

4.3.1. Sensitivity to Reanalysis Forcing

Finally, to assess the sensitivity of our model results to the input snowfall forcing, we forced CICE5 with snowfall data from the MERRA2 reanalysis (all other forcings use JRA55-do expect for snowfall, surface air temperature, and specific humidity). Our CICE5–MERRA2 snowfall simulated snow depth is generally larger than CICE5–JRA55 in June (blue vs. black lines in Figure S3 in Supporting Information S1). Figure S5 in Supporting Information S1 shows the impact of MERRA2 snowfall and surface air cooling/drying on sea ice. Although the anomalous snowfall of MERRA2 during snowstorm events are about 15% larger than JRA55 (Figure S2 in Supporting Information S1), the impact of snowfall on albedo (Figure 8e and Figure S5e in Supporting

Information S1) and SIC (Figures 8g–8h and Figures S5g–S5h in Supporting Information S1) simulated by CICE5–MERRA2 is very similar to those simulated by CICE5–JRA55. MERRA2 snowfall during the summer snowstorm events contributes to increasing the sea ice extent anomaly in late August by up to $\sim 0.5 \times 10^5$ km^2 (black line in Figure S5i in Supporting Information S1) and this is about 30% larger than the sea ice extent anomaly simulated by CICE5–JRA55 snowfall forcing (black line in Figure 8i), although again we expect our JRA55 results to be closer to reality.

Consistent with the relatively weak surface air cooling in MERRA2 compared to JRA55 (Figures 4b and 4d), the MERRA2's surface air effects on late summer SIC and sea ice extent (Figure S5 in Supporting Information S1) are relatively weak: the Arctic sea ice extent anomaly in early September increases by around $\sim 0.8 \times 10^5$ km^2 and this is about 50% small than the sea ice extent anomaly simulated by CICE5–JRA55. These results highlight the high sensitivity of seasonal Arctic sea ice to surface air temperature anomalies.

5. Summary and Conclusions

Using satellite observations and three reanalysis products, this study has shown that Arctic summer snowstorms are accompanied by increasing sea ice extent, increasing surface albedo, and deceasing surface air temperature anomalies over basin-scales. Detailed analysis of surface heat fluxes from CERES indicates that the increased upward shortwave radiation associated with increased surface albedo provides the largest surface heat flux response, followed by increased surface turbulent heat fluxes. Downward longwave and shortwave radiation slightly increase and decrease, respectively, but these changes are relatively small (see Table 3).

Using a forced CICE5-POP2 ice-ocean model framework and various sensitivity experiments, we separated and quantified the potential snowstorm-induced thermal effect and the wind-driven mechanical effect on summer Arctic sea ice from summer snowstorms. Our model simulations indicate that cyclonic wind-driven sea ice drifts results in declines in concentration/albedo in across the Central Arctic, but increases in concentration/albedo around the summer sea ice edge. The thermal response, in contrast, results in increases in SIC around the ice edge providing a greater basin-averaged response. This result is consistent with field observations (Perovich et al., 2017), and further demonstrates the basin-scale response of Arctic sea ice to summer snowstorms as well as the relative importance of the wind-driven dynamic effect and snowfall-induced thermal effect on sea ice. Our study further suggested that the combined impact of summer snowstorms can have a significant influence on the late summer minimum Arctic sea ice extent. Approximately 2–3 snowstorm events occur on average in a given a summer, which our experiments indicate dampened sea ice loss in early September by $\sim 0.2 \times 10^6$ km^2, about 0.4 standard deviations of the interannual variability.

Further model simulations indicate that surface air cooling/drying (and the associated impact on turbulent fluxes) plays a bigger role in mitigating loss of summer Arctic sea ice extent compared to the direct impact of snowfall (and the associated changes to surface albedo and heat capacity) during/after the summer snowstorm events. However, because surface air cooling of JRA55 is larger than AIRS observation and other reanalyzes, the surface air cooling effect is likely to be somewhat overestimated in our CICE5 simulation. Conversely, the snowfall effect on sea ice cover may be underestimated in these model simulations. In CICE5, freshly fallen summer snowfall has limited influence on snow albedo because snow albedo is a function of snow grain radius that is parameterized as a simple function of snow temperature. For a grid cell where the mean snow depth is smaller than 3 cm, snow albedo is a linear function of snow depth. In the case when snow depth is larger 3 cm, snow albedo is not dependent on snow depth because snow deeper than that has reached optical thickness but is a function of snow grain radius (Brandt et al., 2005). In the Delta-Eddington approximation of CICE5, the snow grain radius is set to 125 μm in fresh snow and 1,500 μm in melting snow and is linearly interpolated at surface temperatures between −1.5°C and 0°C (Holland et al., 2012).

Although continuous warming in the Arctic is likely to increase total precipitation by increasing regional surface evaporation (Bintanja & Selten, 2014) and by increasing poleward moisture transport (Kug et al., 2010), snowfall is likely to decrease in the summer because of rapid tropospheric warming (Screen & Simmonds, 2012; R. Zhang et al., 2019). Consistent with Screen and Simmonds (2012), JRA55 and MERRA2 show declines in summer snowfall and snowstorm events (Figure 1), although ERA5 shows no statistically significant trends. Based on our observation-based analysis and model sensitivity experiments, we suggest a better understanding of current and

future summer snowfall, surface air temperature and improved modeling of snow albedo over Arctic sea ice is needed to improve seasonal forecasts and long-term projections of Arctic summer sea ice.

Data Availability Statement

The Clouds and the Earth's Radiant Energy System (CERES) Synoptic 1° × 1° (SYN1deg) product are available at: https://ceres.larc.nasa.gov/data/#syn1deg-level-3. Polar pathfinder sea ice velocity and sea ice concentrations data are both available from the National Snow and Ice Data Center (NSIDC): https://nsidc.org/data/NSIDC-0116/versions/4 and https://nsidc.org/data/G02202/versions/3. The Atmospheric Infrared Sounder on NASA's Aqua satellite (AIRS) data are available at: https://airs.jpl.nasa.gov/data/get-data/standard-data/. Outputs of our CESM2 simulations can be downloaded from Dryad: https://doi.org/10.5061/dryad.4xgxd25c7. Data used in this study are publicly available.

Acknowledgments
We would like to thank two anonymous reviewers for their helpful and constructive comments that greatly improved the manuscript. H.-S. Park and W.-I. Lim are supported by the National Research Foundation of Korea (NRF) 2020R1A2C2010025. This study is also supported by the Korea Meteorological Administration (KMA) Research and Development Program under Grant KMI2020-01114. We also acknowledge computational support from the KMA Supercomputing Center.

References

Aumann, H. H., Chahine, M. T., Gautier, C., Goldberg, M. D., Kalnay, E., McMillin, L. M., et al. (2003). AIRS/AMSU/HSB on the aqua mission: Design, science objectives, data products, and processing systems. *IEEE Transactions on Geoscience and Remote Sensing*, *41*(2), 253–263. https://doi.org/10.1109/TGRS.2002.808356

Barrett, A. P., Stroeve, J. C., & Serreze, M. C. (2020). Arctic Ocean precipitation from atmospheric reanalyses and comparisons with North Pole drifting station records. *Journal of Geophysical Research: Oceans*, *125*(1), e2019JC015415. https://doi.org/10.1029/2019JC015415

Bintanja, R., & Andry, O. (2017). Towards a rain-dominated Arctic. *Nature Climate Change*, *7*(4), 263–267. https://doi.org/10.1038/nclimate3240

Bintanja, R., & Selten, F. M. (2014). Future increases in Arctic precipitation linked to local evaporation and sea-ice retreat. *Nature*, *509*(7501), 479–482. https://doi.org/10.1038/nature13259

Boisvert, L. N., Webster, M. A., Petty, A. A., Markus, T., Bromwich, D. H., & Cullather, R. I. (2018). Intercomparison of precipitation estimates over the Arctic Ocean and its peripheral seas from reanalyses. *Journal of Climate*, *31*(20), 8441–8462. https://doi.org/10.1175/JCLI-D-18-0125.1

Brandt, R. E., Warren, S. G., Worby, A. P., & Grenfell, T. C. (2005). Surface albedo of the Antarctic sea ice zone. *Journal of Climate*, *18*(17), 3606–3622. https://doi.org/10.1175/JCLI3489.1

Briegleb, B. P., & Light, B. (2007). *A Delta-Eddington multiple scattering parameterization for solar radiation in the sea ice component of the Community Climate System Model*. (Tech. Rep. NCAR/TN-472+STR). National Center for Atmospheric Research.

Cabaj, A., Kushner, P. J., Fletcher, C. G., Howell, S., & Petty, A. A. (2020). Constraining reanalysis snowfall over the Arctic Ocean using CloudSat observations. *Geophysical Research Letters*, *47*(4), e2019GL086426. https://doi.org/10.1029/2019GL086426

Cavalieri, D. J., Gloersen, P., & Campbell, W. J. (1984). Determination of sea ice parameters with the NIMBUS 7 SMMR. *Journal of Geophysical Research*, *89*(D4), 5355–5369. https://doi.org/10.1029/JD089ID04P05355

Clancy, R., Bitz, C. M., Blanchard-Wrigglesworth, E., McGraw, M. C., & Cavallo, S. M. (2022). A cyclone-centered perspective on the drivers of asymmetric patterns in the atmosphere and sea ice during Arctic cyclones. *Journal of Climate*, *35*(1), 1–47. https://doi.org/10.1175/JCLI-D-21-0093.1

Comiso, J. C. (1986). Characteristics of Arctic winter sea ice from satellite multispectral microwave observations. *Journal of Geophysical Research*, *91*(C1), 975–994. https://doi.org/10.1029/JC091IC01P00975

Danabasoglu, G., Lamarque, J. F., Bacmeister, J., Bailey, D. A., DuVivier, A. K., Edwards, J., et al. (2020). The community Earth system model version 2 (CESM2). *Journal of Advances in Modeling Earth Systems*, *12*(2), e2019MS001916. https://doi.org/10.1029/2019MS001916

Doelling, D. R., Loeb, N. G., Keyes, D. F., Nordeen, M. L., Morstad, D., Nguyen, C., et al. (2013). Geostationary enhanced temporal interpolation for CERES flux products. *Journal of Atmospheric and Oceanic Technology*, *30*(6), 1072–1090. https://doi.org/10.1175/JTECH-D-12-00136.1

Dong, X., Minnis, P., Xi, B., Sun-Mack, S., & Chen, Y. (2008). Comparison of CERES-MODIS stratus cloud properties with ground-based measurements at the DOE ARM Southern Great Plains site. *Journal of Geophysical Research*, *113*(D3), D03204. https://doi.org/10.1029/2007JD008438

Dou, T., Xiao, C., Liu, J., Han, W., Du, Z., Mahoney, A. R., et al. (2019). A key factor initiating surface ablation of Arctic sea ice: Earlier and increasing liquid precipitation. *The Cryosphere*, *13*(4), 1233–1246. https://doi.org/10.5194/tc-13-1233-2019

Duynkerke, P. G., & de Roode, S. R. (2001). Surface energy balance and turbulence characteristics observed at the SHEBA Ice Camp during FIRE III. *Journal of Geophysical Research*, *106*(D14), 15313–15322. https://doi.org/10.1029/2000JD900537

Ebert, E. E., & Curry, J. A. (1993). An intermediate one-dimensional thermodynamic sea ice model for investigating ice-atmosphere interactions. *Journal of Geophysical Research*, *98*(6), 10085–10109. https://doi.org/10.1029/93jc00656

Ehn, J. K., Granskog, M. A., Papakyriakou, T., Galley, R., & Barber, D. G. (2006). Surface albedo observations of Hudson Bay (Canada) landfast sea ice during the spring melt. In *Annals of glaciology* (Vol. 44, pp. 23–29). Cambridge University Press. https://doi.org/10.3189/172756406781811376

Feltham, D. L., Untersteiner, N., Wettlaufer, J. S., & Worster, M. G. (2006). Sea ice is a mushy layer. *Geophysical Research Letters*, *33*(14), L14501. https://doi.org/10.1029/2006GL026290

Fetterer, F., Knowles, K., Meier, W. N., Savoie, M., & Windnagel, A. K. (2017). *Sea Ice index*, Version 3. National Snow and Ice Data Center (NSIDC).

Gelaro, R., McCarty, W., Suárez, M. J., Todling, R., Molod, A., Takacs, L., et al. (2017). The modern-era retrospective analysis for research and applications, version 2 (MERRA-2). *Journal of Climate*, *30*(14), 5419–5454. https://doi.org/10.1175/JCLI-D-16-0758.1

Goosse, H., Kay, J. E., Armour, K. C., Bodas-Salcedo, A., Chepfer, H., Docquier, D., et al. (2018). Quantifying climate feedbacks in polar regions. *Nature Communications*, *9*(1), 1–13. https://doi.org/10.1038/s41467-018-04173-0

Grenfell, T. C., & Maykut, G. A. (1977). The optical properties of ice and snow in the Arctic Basin. *Journal of Glaciology*, *18*(80), 445–463. https://doi.org/10.3189/s0022143000021122

Griffies, S. M., Biastoch, A., Böning, C., Bryan, F., Danabasoglu, G., Chassignet, E. P., et al. (2009). Coordinated ocean-ice reference experiments (COREs). *Ocean Modelling*, *26*(1–2), 1–46. https://doi.org/10.1016/j.ocemod.2008.08.007

Griffies, S. M., Danabasoglu, G., Durack, P. J., Adcroft, A. J., Balaji, V., Böning, C. W., et al. (2016). OMIP contribution to CMIP6: Experimental and diagnostic protocol for the physical component of the Ocean Model Intercomparison Project. *Geoscientific Model Development*, *9*(9), 3231–3296. https://doi.org/10.5194/gmd-9-3231-2016

Hersbach, H., Bell, B., Berrisford, P., Hirahara, S., Horányi, A., Muñoz-Sabater, J., et al. (2020). The ERA5 global reanalysis. *Quarterly Journal of the Royal Meteorological Society*, *146*(730), 1999–2049. https://doi.org/10.1002/qj.3803

Hezel, P. J., Zhang, X., Bitz, C. M., Kelly, B. P., & Massonnet, F. (2012). Projected decline in spring snow depth on Arctic sea ice caused by progressively later autumn open ocean freeze-up this century. *Geophysical Research Letters*, *39*(17), L17505. https://doi.org/10.1029/2012GL052794

Holland, M. M., Bailey, D. A., Briegleb, B. P., Light, B., & Hunke, E. (2012). Improved sea ice shortwave radiation physics in CCSM4: The impact of melt ponds and aerosols on Arctic sea ice. *Journal of Climate*, *25*(5), 1413–1430. https://doi.org/10.1175/JCLI-D-11-00078.1

Huang, Y., Taylor, P. C., Rose, F. G., Rutan, D. A., Shupe, M. D., Webster, M. A., & Smith, M. M. (2022). Toward a more realistic representation of surface albedo in NASA CERES-derived surface radiative fluxes: A comparison with the MOSAiC field campaign: Comparison of CERES and MOSAiC surface radiation fluxes. *Elementa: Science of the Anthropocene*, *10*(1), 00013. https://doi.org/10.1525/ELEMENTA.2022.00013

Hunke, E. C., Hebert, D. A., & Lecomte, O. (2013). Level-ice melt ponds in the Los Alamos sea ice model, CICE. *Ocean Modelling*, *71*, 26–42. https://doi.org/10.1016/j.ocemod.2012.11.008

Hunke, E. C., Lipscomb, W. H., Turner, A. K., Jeffery, N., & Elliot, S. (2015). *CICE: The Los Alamos sea ice model documentation and software user's manual version 5.1 LA-CC-06-012*. (Vol. 675, pp. 500). T-3 Fluid Dynamics Group Los Alamos National Laboratory.

Jin, Z., Charlock, T. P., Yang, P., Xie, Y., & Miller, W. (2008). Snow optical properties for different particle shapes with application to snow grain size retrieval and MODIS/CERES radiance comparison over Antarctica. *Remote Sensing of Environment*, *112*(9), 3563–3581. https://doi.org/10.1016/J.RSE.2008.04.011

Kay, J. E., L'Ecuyer, T., Gettelman, A., Stephens, G., & O'Dell, C. (2008). The contribution of cloud and radiation anomalies to the 2007 Arctic sea ice extent minimum. *Geophysical Research Letters*, *35*(8), L08503. https://doi.org/10.1029/2008GL033451

Kobayashi, S., Ota, Y., Harada, Y., Ebita, A., Moriya, M., Onoda, H., et al. (2015). The JRA-55 reanalysis: General specifications and basic characteristics. *Journal of the Meteorological Society of Japan*, *93*(1), 5–48. https://doi.org/10.2151/jmsj.2015-001

Koster, R. D., Bosilovich, M. G., Akella, S., Lawrence, C., Cullather, R., Draper, C., et al. (2015). MERRA-2: Initial evaluation of the climate. In *NASA Tech. Rep. Series on Global Modeling and Data Assimilation*, (Vol. 43, p. 153). NASA/TM-2015-104606. NASA.

Kug, J.-S., Choi, D.-H., Jin, F.-F., Kwon, W.-T., & Ren, H.-L. (2010). Role of synoptic eddy feedback on polar climate responses to the anthropogenic forcing. *Geophysical Research Letters*, *37*(14), L14704. https://doi.org/10.1029/2010GL043673

Lim, W.-I., Park, H.-S., Stewart, A. L., & Seo, K.-H. (2022). Suppression of Arctic sea ice growth in the Eurasian–Pacific seas by winter clouds and snowfall. *Journal of Climate*, *35*(2), 669–686. https://doi.org/10.1175/JCLI-D-21-0282.1

Lukovich, J. V., Stroeve, J., Crawford, A., Hamilton, L., Tsamados, M., Heorton, H., & Massonnet, F. (2021). Summer extreme cyclone impacts on Arctic sea ice. *Journal of Climate*, *34*(12), 1–54. https://doi.org/10.1175/JCLI-D-19-0925.1

Meier, W. N., Fetterer, F., Savoie, M., Mallory, S., Duerr, R., & Stroeve, J. (2017). *NOAA/NSIDC climate data record of passive microwave sea ice concentration*, Version 3. NSIDC: National Snow and Ice Data Center. https://doi.org/10.7265/N59P2ZTG

Minnis, P., Sun-Mack, S., Young, D. F., Heck, P. W., Garber, D. P., Chen, Y., et al. (2011). CERES edition-2 cloud property retrievals using TRMM VIRS and Terra and Aqua MODIS data—Part I: Algorithms. *IEEE Transactions on Geoscience and Remote Sensing*, *49*(11), 4374–4400. https://doi.org/10.1109/TGRS.2011.2144601

Park, H.-S., & Stewart, A. L. (2016). An analytical model for wind-driven Arctic summer sea ice drift. *The Cryosphere*, *10*(1), 227–244. https://doi.org/10.5194/tc-10-227-2016

Parkinson, C. L., & Washington, W. M. (1979). A large-scale numerical model of sea ice. *Journal of Geophysical Research*, *84*(C1), 311–337. https://doi.org/10.1029/JC084IC01P00311

Perovich, D. K., Grenfell, T. C., & Hobbs, P. V. (2002). Seasonal evolution of the albedo of multiyear Arctic sea ice. *Journal of Geophysical Research*, *107*(C10), 8044. https://doi.org/10.1029/2000JC000438

Perovich, D. K., & Polashenski, C. (2012). Albedo evolution of seasonal Arctic sea ice. *Geophysical Research Letters*, *39*(8), L08501. https://doi.org/10.1029/2012GL051432

Perovich, D. K., Polashenski, C., Arntsen, A., & Stwertka, C. (2017). Anatomy of a late spring snowfall on sea ice. *Geophysical Research Letters*, *44*(6), 2802–2809. https://doi.org/10.1002/2016GL071470

Petty, A. A., Holland, M. M., Bailey, D. A., & Kurtz, N. T. (2018). Warm Arctic, increased winter sea ice growth? *Geophysical Research Letters*, *45*(23), 12922–12930. https://doi.org/10.1029/2018GL079223

Petty, A. A., Schröder, D., Stroeve, J. C., Markus, T., Miller, J., Kurtz, N. T., et al. (2017). Skillful spring forecasts of September Arctic sea ice extent using passive microwave sea ice observations. *Earth's Future*, *5*(2), 254–263. https://doi.org/10.1002/2016EF000495

Riihelä, A., Key, J. R., Meirink, J. F., Kuipers Munneke, P., Palo, T., & Karlsson, K. G. (2017). An intercomparison and validation of satellite-based surface radiative energy flux estimates over the Arctic. *Journal of Geophysical Research: Atmospheres*, *122*(9), 4829–4848. https://doi.org/10.1002/2016JD026443

Rinke, A., Segger, B., Crewell, S., Maturilli, M., Naakka, T., Nygård, T., et al. (2019). Trends of vertically integrated water vapor over the Arctic during 1979–2016: Consistent moistening all over? *Journal of Climate*, *32*(18), 6097–6116. https://doi.org/10.1175/JCLI-D-19-0092.1

Schreiber, E. A. P., & Serreze, M. C. (2020). Impacts of synoptic-scale cyclones on Arctic sea-ice concentration: A systematic analysis. *Annals of Glaciology*, *61*(82), 139–153. https://doi.org/10.1017/aog.2020.23

Schröder, D., Feltham, D. L., Flocco, D., & Tsamados, M. (2014). September Arctic sea-ice minimum predicted by spring melt-pond fraction. *Nature Climate Change*, *4*(5), 353–357. https://doi.org/10.1038/nclimate2203

Screen, J. A., & Simmonds, I. (2012). Declining summer snowfall in the Arctic: Causes, impacts and feedbacks. *Climate Dynamics*, *38*(11–12), 2243–2256. https://doi.org/10.1007/s00382-011-1105-2

Screen, J. A., Simmonds, I., & Keay, K. (2011). Dramatic interannual changes of perennial Arctic sea ice linked to abnormal summer storm activity. *Journal of Geophysical Research*, *116*(D15), D15105. https://doi.org/10.1029/2011JD015847

Sepp, M., & Jaagus, J. (2010). Changes in the activity and tracks of Arctic cyclones. *Climatic Change*, *105*(3), 577–595. https://doi.org/10.1007/S10584-010-9893-7

Serreze, M. C., & Barrett, A. P. (2008). The summer cyclone maximum over the central Arctic Ocean. *Journal of Climate*, *21*(5), 1048–1065. https://doi.org/10.1175/2007JCLI1810.1

Serreze, M. C., & Barry, R. G. (2014). *The Arctic climate system. Cambridge atmospheric and space science series* (2nd ed.). Cambridge University Press. https://doi.org/10.1017/CBO9781139583817

Serreze, M. C., Barry, R. G., & Walsh, J. E. (1995). Atmospheric water vapor characteristics at 70°N. *Journal of Climate*, *8*(4), 719–731. https://doi.org/10.1175/1520-0442(1995)008<0719:awvca>2.0.co;2

Shalina, E. V., & Sandven, S. (2018). Snow depth on Arctic sea ice from historical in situ data. *The Cryosphere*, *12*(6), 1867–1886. https://doi.org/10.5194/tc-12-1867-2018

Simmonds, I., Burke, C., & Keay, K. (2008). Arctic climate change as manifest in cyclone behavior. *Journal of Climate*, *21*(22), 5777–5796. https://doi.org/10.1175/2008JCLI2366.1

Smith, R., Jones, P., Briegleb, B., Bryan, F., Danabasoglu, G., Dennis, J., et al. (2010). *The Parallel Ocean Program (POP) reference manual*. Technical report, Los Alamos National Laboratory.

Suarez, M. J., Rienecker, M. M., Todling, R., Bacmeister, J., Takacs, L., Liu, H. C., et al. (2008). The GEOS-5 data assimilation system-documentation of versions 5.0.1, 5.1.0, and 5.2.0. In M. J. Suarez (Ed.). *Technical report series on global modeling and data assimilation* (Vol. 27). NASA tech. Memo. NASA/TM-2008-104606. NASA Goddard Space Flight Center.

Sumata, H., Kwok, R., Gerdes, R., Kauker, F., & Karcher, M. (2015). Uncertainty of Arctic summer ice drift assessed by high-resolution SAR data. *Journal of Geophysical Research: Oceans*, *120*(8), 5285–5301. https://doi.org/10.1002/2015JC010810

Sumata, H., Lavergne, T., Girard-Ardhuin, F., Kimura, N., Tschudi, M., Kauker, F., et al. (2014). An intercomparison of Arctic ice drift products to deduce uncertainty estimates. *Journal of Geophysical Research: Oceans*, *119*(8), 4887–4921. https://doi.org/10.1002/2013jc009724

Tschudi, M., Meier, W. N., & Stewart, J. S. (2020). An enhancement to sea ice motion and age products at the National Snow and Ice Data Center (NSIDC). *The Cryosphere*, *14*(5), 1519–1536. https://doi.org/10.5194/tc-14-1519-2020

Tschudi, M. A., Meier, W. N., Stewart, J. S., Fowler, C., & Maslanik, J. (2019). *Polar pathfinder daily 25 km EASE-grid sea ice motion vectors*, version 4. National Snow and Ice Data Center Distributed Active Archive Center, NASA. https://doi.org/10.5067/INAWUWO7QH7B

Tsujino, H., Urakawa, S., Nakano, H., Small, R. J., Kim, W. M., Yeager, S. G., et al. (2018). JRA-55 based surface dataset for driving ocean–sea-ice models (JRA55-do). *Ocean Modelling*, *130*, 79–139. https://doi.org/10.1016/j.ocemod.2018.07.002

Turner, A. K., & Hunke, E. C. (2015). Impacts of a mushy-layer thermodynamic approach in global sea-ice simulations using the CICE sea-ice model. *Journal of Geophysical Research: Oceans*, *120*(2), 1253–1275. https://doi.org/10.1002/2014JC010358

Uttal, T., Curry, J. A., Mcphee, M. G., Perovich, D. K., Moritz, R. E., Maslanik, J. A., et al. (2002). Surface heat budget of the Arctic Ocean. *Bulletin of the American Meteorological Society*, *83*(2), 255–275. https://doi.org/10.1175/1520-0477(2002)083<0255:SHBOTA>2.3.CO;2

Walsh, J. E. (2014). Intensified warming of the Arctic: Causes and impacts on middle latitudes. *Global and Planetary Change*, *117*, 52–63. https://doi.org/10.1016/J.GLOPLACHA.2014.03.003

Warren, S. G., Rigor, I. G., Untersteiner, N., Radionov, V. F., Bryazgin, N. N., Aleksandrov, Y. I., & Colony, R. (1999). Snow depth on Arctic sea ice. *Journal of Climate*, *12*(6), 1814–1829. https://doi.org/10.1175/1520-0442(1999)012<1814:SDOASI>2.0.CO;2

Webster, M. A., Gerland, S., Holland, M., Hunke, E., Kwok, R., Lecomte, O., et al. (2018). Snow in the changing sea-ice systems. *Nature Climate Change*, *8*(11), 946–953. https://doi.org/10.1038/s41558-018-0286-7

Webster, M. A., Parker, C., Boisvert, L., & Kwok, R. (2019). The role of cyclone activity in snow accumulation on Arctic sea ice. *Nature Communications*, *10*(1), 5285. https://doi.org/10.1038/s41467-019-13299-8

Wu, X., Budd, W. F., Lytle, V. I., Massom, R. A., & Budd, W. F. (1999). The effect of snow on Antarctic sea ice simulations in a coupled atmosphere-sea ice model. *Climate Dynamics*, *15*(2), 127–143. https://doi.org/10.1007/s003820050272

Zhang, R., Wang, H., Fu, Q., Rasch, P. J., & Wang, X. (2019). Unraveling driving forces explaining significant reduction in satellite-inferred Arctic surface albedo since the 1980s. *Proceedings of the National Academy of Sciences of the United States of America*, *116*(48), 23947–23953. https://doi.org/10.1073/PNAS.1915258116

Zhang, X., Walsh, J. E., Zhang, J., Bhatt, U. S., & Ikeda, M. (2004). Climatology and interannual variability of Arctic cyclone activity: 1948–2002. *Journal of Climate*, *17*(12), 2300–2317. https://doi.org/10.1175/1520-0442(2004)017<2300:CAIVOA>2.0.CO;2